Petrostructural and Geochronological Constraints on Devonian Extension-Shortening Cycle in the Chinese Altai: Implications for Retreating-Advancing Subduction

Lingzhu Kong, Yingde Jiang, Karel Schulmann, Jian Zhang, Roberto F. Weinberg, Min Sun, Sheng Wang, Tan Shu, Jun Ning

▶ **To cite this version:**

Lingzhu Kong, Yingde Jiang, Karel Schulmann, Jian Zhang, Roberto F. Weinberg, et al.. Petrostructural and Geochronological Constraints on Devonian Extension-Shortening Cycle in the Chinese Altai: Implications for Retreating-Advancing Subduction. Tectonics, 2022, 41 (9), 10.1029/2021TC007195 . hal-04222092

HAL Id: hal-04222092
https://hal.science/hal-04222092

Submitted on 7 Dec 2023

HAL is a multi-disciplinary open access archive for the deposit and dissemination of scientific research documents, whether they are published or not. The documents may come from teaching and research institutions in France or abroad, or from public or private research centers.

L'archive ouverte pluridisciplinaire **HAL**, est destinée au dépôt et à la diffusion de documents scientifiques de niveau recherche, publiés ou non, émanant des établissements d'enseignement et de recherche français ou étrangers, des laboratoires publics ou privés.

Copyright

Check for updates

Tectonics®

RESEARCH ARTICLE
10.1029/2021TC007195

Key Points:

- Crustal extension in the Chinese Altai formed a sub-horizontal high-temperature/low-pressure fabric at Early-Middle Devonian
- Middle Devonian upright folding accounted for shortening of heterogeneously extended, partially molten and stratified crust
- Multiple shortening-extension cycles as proxies of alternating retreats and advances of subduction system governed evolution of Altai

Supporting Information:

Supporting Information may be found in the online version of this article.

Correspondence to:

Y. D. Jiang,
jiangyd@gig.ac.cn

Citation:

Kong, L., Jiang, Y., Schulmann, K., Zhang, J., Weinberg, R. F., Sun, M., et al. (2022). Petrostructural and geochronological constraints on Devonian extension-shortening cycle in the Chinese Altai: Implications for retreating-advancing subduction. *Tectonics*, *41*, e2021TC007195. https://doi.org/10.1029/2021TC007195

Received 7 JAN 2022
Accepted 17 AUG 2022

Author Contributions:

Conceptualization: Lingzhu Kong
Data curation: Lingzhu Kong
Formal analysis: Lingzhu Kong
Investigation: Lingzhu Kong
Writing – original draft: Lingzhu Kong
Writing – review & editing: Lingzhu Kong

© 2022. American Geophysical Union. All Rights Reserved.

Petrostructural and Geochronological Constraints on Devonian Extension-Shortening Cycle in the Chinese Altai: Implications for Retreating-Advancing Subduction

Lingzhu Kong[1,2,3], Yingde Jiang[1,2], Karel Schulmann[4,5], Jian Zhang[6,7], Roberto F. Weinberg[8], Min Sun[9], Sheng Wang[10], Tan Shu[1,2,3], and Jun Ning[1,2,3]

[1]State Key Laboratory of Isotope Geochemistry, Guangzhou Institute of Geochemistry, Chinese Academy of Sciences, Guangzhou, China, [2]CAS Center for Excellence in Deep Earth Science, Guangzhou, China, [3]University of Chinese Academy of Sciences, Beijing, China, [4]Centre for Lithospheric Research, Czech Geological Survey, Prague, Czech Republic, [5]Université de Strasbourg, CNRS, ITES UMR 7063, Strasbourg, France, [6]Guangdong Provincial Key Laboratory of Mineral Resources & Geological Processes, School of Earth Sciences and Engineering, Sun Yat-sen University, Guangzhou, China, [7]Southern Marine Science and Engineering Guangdong Laboratory (Zhuhai), Zhuhai, China, [8]School of Earth, Atmosphere and Environment, Monash University, Clayton, VIC, Australia, [9]Department of Earth Sciences, The University of Hong Kong, Hong Kong, China, [10]School of Civil Engineering, Anhui Jianzhu University, Hefei, China

Abstract Structural and metamorphic effects of a Devonian extension-shortening cycle in the NW Chinese Altai were investigated using combined structural-petrological analysis and zircon and monazite U-Pb geochronology. Structural observations revealed a ubiquitous, sub-horizontal metamorphic fabric (S1), which was originally sub-parallel with horizontal bedding (S0) of supracrustal Devonian volcanic-sedimentary basins. This metamorphic fabric is defined by a sillimanite-bearing migmatitic gneissosity associated with extensional shear bands and a cordierite-bearing schistosity in the orogenic lower and middle crust, respectively. Staurolite relics preserved in the S1 fabric are interpreted as relics of older, higher pressure Barrovian-type metamorphism. These structural-metamorphic features are correlated with decompression and heating and interpreted as reflecting a crustal-scale extensional phase. S1 was folded to form N-S-oriented upright antiforms cored by migmatites and locally transposed by steep S2 foliation during a ~W-E-directed shortening (in current coordinates). Andalusite and cordierite overgrew the migmatitic S2 foliation attesting to decreasing pressure associated with vertical extrusion of migmatites in cores of F2 antiforms. New U-Pb age data from subhorizontally foliated migmatites suggest that the D1 extension started at least before ~410 Ma. Age data of syn-D2 granite intrusions and dykes constrain the D2 shortening starting soon after D1 extension and ending at ~378 Ma. Combined with regional data, cycles of extensional and contractional tectonic regimes can be defined, which also show eastward migration along-strike of the Altai range. Such extension-shortening cycles could result from alternating retreating and advancing subduction, which governed the evolution of the Altai accretionary system from the Ordovician until the Carboniferous.

1. Introduction

It is generally accepted that variations in advancing and retreating subduction modes control the tectonic styles of Pacific-type orogenic systems (Cawood et al., 2009; Collins, 2002a; Collins & Richards, 2008). Advancing of the overriding plate above the hinge of the downgoing slab tends to induce strong mechanical coupling, leading to crustal thickening and formation of retro-arc foreland basins, whereas retreating of the downgoing slab hinge (also known as rollback) with respect to the overriding plate is likely to cause gravitational collapse leading to crustal thinning, arc splitting, and development of arc-back-arc systems (Collins, 2002b; Lister & Forster, 2009). These changes in relative plate motion lead to tectonic mode switches characterized by a shift from horizontal extension to horizontal shortening as exemplified by the tectonic evolution of the Andes or southwest Pacific (Cawood et al., 2009). While the retreating mode is responsible for growth of the continental crust owning to addition of juvenile magmatic products and building of volcanic-sedimentary edifice (Cawood et al., 2009; Collins, 2002a), the advancing mode plays a fundamental role in the accretion and subsequent stabilization of juvenile crustal components (Cawood et al., 2009; Foster et al., 2009; Glen, 2013; Kemp et al., 2009). While the roles and impacts of the different modes are clear, the identification of them in fossil orogenic belts is not always straightforward because the accretionary geological records, in particular the structural and metamorphic effects, are often obliterated by subsequent collisional processes following closure of oceanic domains.

19449194, 2022, 9, Downloaded from https://agupubs.onlinelibrary.wiley.com/doi/10.1029/2021TC007195 by Portail BibCNRS INSU, Wiley Online Library on [06/12/2023]. See the Terms and Conditions (https://onlinelibrary.wiley.com/terms-and-conditions) on Wiley Online Library for rules of use; OA articles are governed by the applicable Creative Commons License

As the largest known Phanerozoic accretionary orogenic system on Earth, the Central Asian Orogenic Belt (CAOB) has long been interpreted to have a tectonic evolution analogous to the modern southwest Pacific (Windley et al., 2007; Xiao et al., 2018). It is generally accepted that the formation of the CAOB reflects long-lived oceanic subduction (Şengör et al., 1993). Two main stages of subduction zone retreat have been recorded in the eastern CAOB and dated at Ordovician and Devonian, respectively: (a) the Ordovician retreating stage marked by the formation of the ~1,800-km long Ikh-Mongol Arc System (Janoušek et al., 2018) and a coeval turbidite basin forming the ~2,500-km long Altai accretionary wedge (Janoušek et al., 2018; Jiang et al., 2017) and (b) the Devonian retreat stage inferred from the unprecedented amount of Devonian magmatism affecting the southern part of the Altai accretionary wedge (Cai et al., 2011b; Cui et al., 2020; Jiang et al., 2011b; Li et al., 2019; Wang et al., 2006) in association with a drift of zircon Hf isotopic compositions toward much less evolved values in granitoids (Li et al., 2019; Sun et al., 2009). This Devonian retreat has been repeatedly documented in recent years but the related tectono-metamorphic evolution and structural patterns remain obscure. The succession of Devonian structures and metamorphism has recently been described and dated (Broussolle et al., 2018; Jiang et al., 2019; Xu et al., 2021; Zhang et al., 2015), however, the effects of Permian deformation related to the collision of the Chinese Altai with the southerly Junggar arc domain (Jiang et al., 2019; Li et al., 2017; Xu et al., 2021) complicates their restorations (Guy et al., 2020, 2021).

In this contribution, a representative area of the Jiadengyu region at the NW Chinese Altai is investigated by means of combined petrostructural and petro-chronological analyses. This region is characterized by almost absent Permian deformation and therefore the earlier tectonic and metamorphic history can be constrained. The resultant data are synthesized to characterize geometries, kinematics, and timing of succession of extensional and compressional Devonian fabrics. This work provides constraints on the Devonian tectonic switch that can be extrapolated to other regions of Altai Orogen and used as a proxy of the Paleozoic supra-subduction model of the eastern tract of the CAOB.

2. Geological Setting

2.1. Regional Geological Background

The CAOB (Figure 1) was formed by multiple accretion and amalgamation of diverse terranes, including island arcs, ophiolites, oceanic islands, seamounts, accretionary wedges, and microcontinents, from ca. 1,000 to 230 Ma (Şengör et al., 1993; Sengör & Natal'in, 1996; Windley et al., 2007). These tectonic units were interpreted as orogenic components of a single "Kipchak" arc by Şengör et al. (1993). More recently, Xiao et al. (2015) subdivided the CAOB into three collage systems represented by the Mongolian Collage in the east, the Kazakhstan Collage in the west, and the Tarim-North China Collage in the south. These three collage systems have been considered to have experienced contrasting geodynamic evolution through the Neoproterozoic to the Paleozoic before their final amalgamation during the Permian and Early Triassic.

The Mongolian Collage is stitched with the Siberian Craton by the ca. 500 Ma Sayan-Baikal metamorphic belt in the north (Donskaya et al., 2000; Gladkochub et al., 2008), and separated from the North China Craton by the Late Permian to Early Triassic Solonker suture zone in the south (Eizenhofer et al., 2014; Xiao et al., 2003). This collage is composed of Precambrian continental ribbons (collectively known as the Tuva-Mongolian continental ribbons), and their peripheral Neoproterozoic-Early Paleozoic arcs (the Lake Zone) and accretionary complexes (the Hovd-Altai Zone) in the north (Kröner et al., 2010; Soejono et al., 2016), and oceanic domains of predominantly Devonian-Carboniferous ages (the East Junggar and Trans-Altai Zone) in the south (Figure 1b, Lehmann et al., 2010). The Altai accretionary system represents a more than 2,000-km long-chain rimming the southwestern margin of the Tuva-Mongolian continental ribbons. It consists mainly of two major units: (a) a Cambro-Ordovician arc developed on the southern border of the Mongolian continental blocks (known as the Ikh-Mongol Arc, Janoušek et al., 2018), and (b) a coeval accretionary wedge composed mainly of a graywacke-dominated sequence associated with less extensive oceanic crustal fragments known as the Altai accretionary wedge (Jiang et al., 2017; Xiao et al., 2009).

The Altai accretionary wedge extends from Russia in the west, through northwestern China, to west Mongolia in the east. Its Chinese segment called the Chinese Altai is separated from the Devono-Carboniferous Junggar arc by the NW-trending Erqis Fault (Figure 1) (Jiang et al., 2011a; Xiao et al., 2009). The Chinese Altai was traditionally regarded to be composed of five major NW-SE trending tectonostratigraphic "terranes" separated by sub-parallel

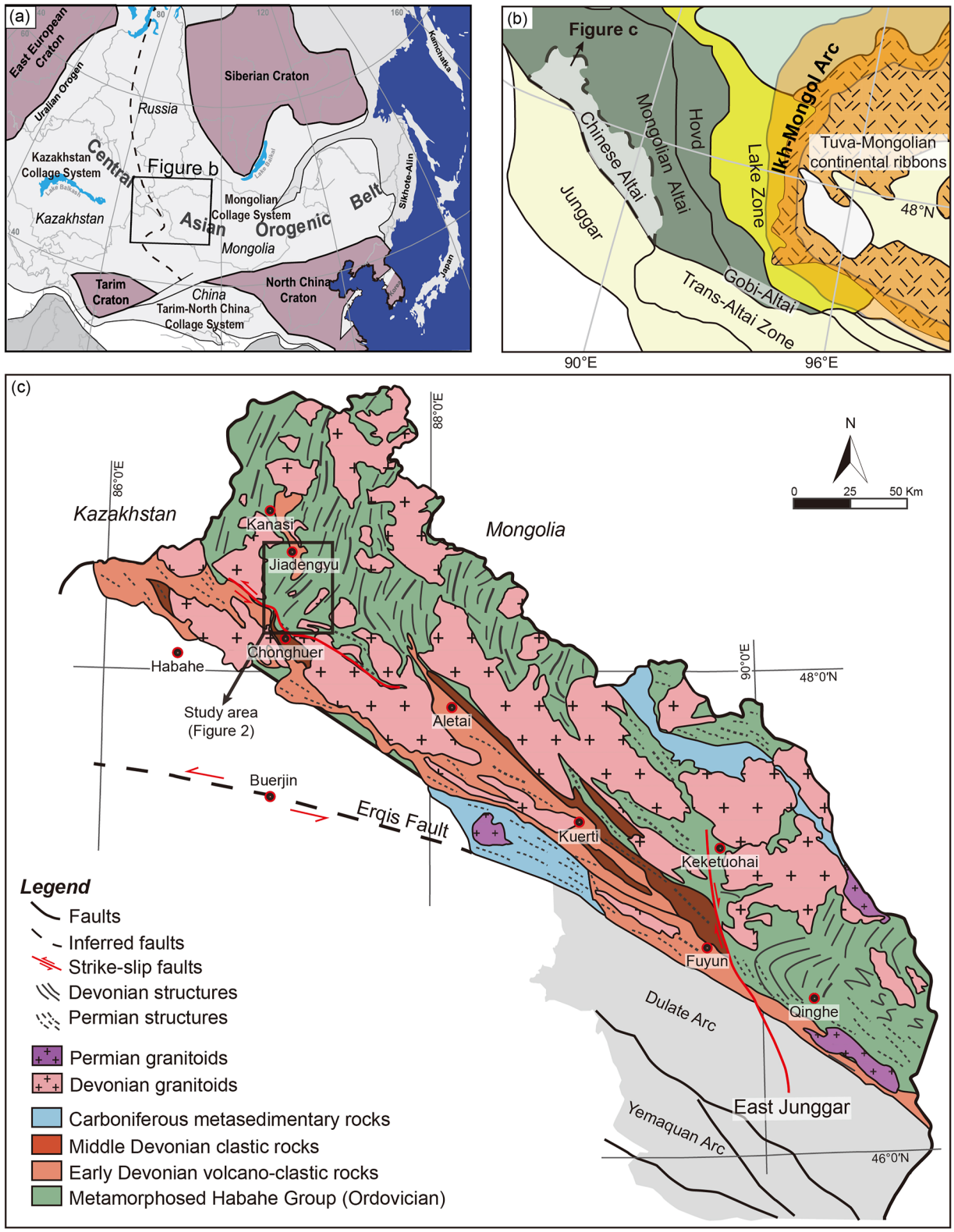

Figure 1. Simplified geological map of (a) the Central Asian Orogenic Belt (CAOB) (modified after Windley & Xiao, 2018), (b) the Mongolian Collage System (modified after Jiang et al., 2017), and (c) the Chinese Altai (modified after Broussolle et al., 2018). Main lithostratigraphic units and strikes of main structures of the Chinese Altai are also indicated.

19449194, 2022, 9, Downloaded from https://agupubs.onlinelibrary.wiley.com/doi/10.1029/2021TC007195 by Portail BibCNRS INSU, Wiley Online Library on [06/12/2023]. See the Terms and Conditions (https://onlinelibrary.wiley.com/terms-and-conditions) on Wiley Online Library for rules of use; OA articles are governed by the applicable Creative Commons License

faults (Windley et al., 2002). However, based on lithostratigraphy, magmatic, metamorphic, and structural correlations, it has been proposed that the Chinese Altai apparent "terrane" architecture resulted from a superposition of Silurian-Devonian and Permian-Triassic tectono-thermal cycles (Broussolle et al., 2019; Zhang et al., 2015).

The Silurian-Devonian and Permian-Triassic events responsible for the final architecture of the Chinese Altai have been subjects of many studies in the last decade. The Silurian-Devonian event is characterized by the widespread occurrence of 420-370 Ma granitoids that occupy more than 40% of the map surface of the Chinese Altai (Cai et al., 2011b; Huang et al., 2020; Jiang et al., 2016; Sun et al., 2008; Wang et al., 2006; Yu et al., 2017; Yuan et al., 2007). Magmatism is associated with extensive anatexis and high-temperature metamorphism of fertile sediments (Broussolle et al., 2018; Jiang et al., 2011b, 2015, 2019; Long et al., 2007; Zhang et al., 2015), which led to the transformation of the Altai accretionary wedge into a mature and layered orogenic crust. This crust consists of: (a) an up to granulite-facies partially molten orogenic lower crust at 25–35 km depth, (b) a greenschist- to amphibolite-facies metamorphosed sedimentary sequence comprising the orogenic middle crust, and (c) an up to 8 km thick, low-grade to un-metamorphosed orogenic upper crust composed mainly of Devonian (meta)volcano-clastic succession (Broussolle et al., 2019; Jiang et al., 2019; Wang et al., 2021).

The Permian-Triassic event was also extensive but affected mainly the southern Chinese Altai (Jiang et al., 2019; Li et al., 2016, 2017). It is expressed by the extrusion of migmatites and granulites parallel to the contact between the Chinese Altai and the Junggar arc, associated with top-to-south thrusting, NW-SE-trending upright folding, and NW-SE-trending strike-slip movement (Broussolle et al., 2018; Jiang et al., 2019; Li et al., 2016, 2017). This event was also associated with felsic and mafic magmatism (Cai et al., 2011b; Shu et al., 2022; Tong et al., 2006), which has been collectively considered to be related to the Permian Chinese Altai-East Junggar collision (e.g., Li et al., 2017; Jiang et al., 2019, 2022).

2.2. Geology of the Study Area

This study focus on a ca. 40 * 40 km^2 region (Figure 2) of the Jiadengyu area in the northwestern Chinese Altai (Figure 1). It is composed mainly of the metamorphosed Ordovician Habahe Group associated with subordinate Early-Middle Devonian volcano-clastic rocks in the north and south. The Ordovician Habahe Group represents the oldest sedimentary sequence of the Altai wedge in the Chinese Altai (Long et al., 2008). It consists mainly of thick graywacke-dominated clastic to volcano-clastic sedimentary rocks that are variously metamorphosed under lower greenschist- to amphibolite-facies conditions forming phyllite, greenschist, mica schist, and paragneiss in the field. Detrital zircons from the Habahe Group rocks showed major age peaks in a range of 520-480 Ma, and the youngest age population around 460 Ma (Long et al., 2007). The medium-grade metamorphosed Habahe Group alternates with upper amphibolite-facies migmatitic units which were traditionally taken as Precambrian basement rocks but have been reinterpreted as high-grade metamorphic equivalents of the Habahe Group (Cai et al., 2011b; Jiang et al., 2011a; Sun et al., 2008). Metamorphic zircons from these migmatitic portions yielded U-Pb ages of ca. 390 Ma, interpreted as the timing of high-temperature metamorphism and migmatization (Jiang et al., 2011b).

The Habahe Group is overlain by an Early Devonian low-grade volcano-clastic sequence known as the Dongxileke Formation in the north and less extensive Middle Devonian siliciclastic sediments, fossiliferous limestones, and volcano-clastic rocks of the Altai Formation in the south (Figure 2). The Dongxileke Formation is composed mainly of rhyolite and andesite with calc-alkaline affinity (Long et al., 2012; Shan et al., 2005). Zircons from the rhyolite yielded a 411 $\pm$ 4 Ma U-Pb age interpreted as the timing of volcanic eruption (Wang et al., 2011). Likewise, felsic meta-volcanic rocks from the Altai Formation gave zircon ages of 407-383 Ma, documenting the presence of Middle Devonian magmatism (Zhang et al., 2015).

Abundant granitoids associated with minor mafic intrusions occur in the study area. These rocks were emplaced during two main phases. The first phase is characterized by the emplacement of isolated small rounded mafic and felsic bodies. These rocks have similar emplacement ages of 480-460 Ma (Cai et al., 2011b; Han et al., 2016; Sun et al., 2009; Zhao et al., 2018). Some of them exhibit arc-related geochemical characteristics (Cai, Sun, Yuan, et al., 2011). The second phase of magmatism formed many km- to dozens of km-scale granitoid plutons in the region. These plutons are predominantly two-mica granites and/or biotite granodiorites, with metaluminous to peraluminous compositions (Cai et al., 2011a; Sun et al., 2008). Geochronological investigations revealed that

19449194, 2022, 9, Downloaded from https://agupubs.onlinelibrary.wiley.com/doi/10.1029/2021TC007195 by Portail BibCNRS INSU, Wiley Online Library on [06/12/2023]. See the Terms and Conditions (https://onlinelibrary.wiley.com/terms-and-conditions) on Wiley Online Library for rules of use; OA articles are governed by the applicable Creative Commons License

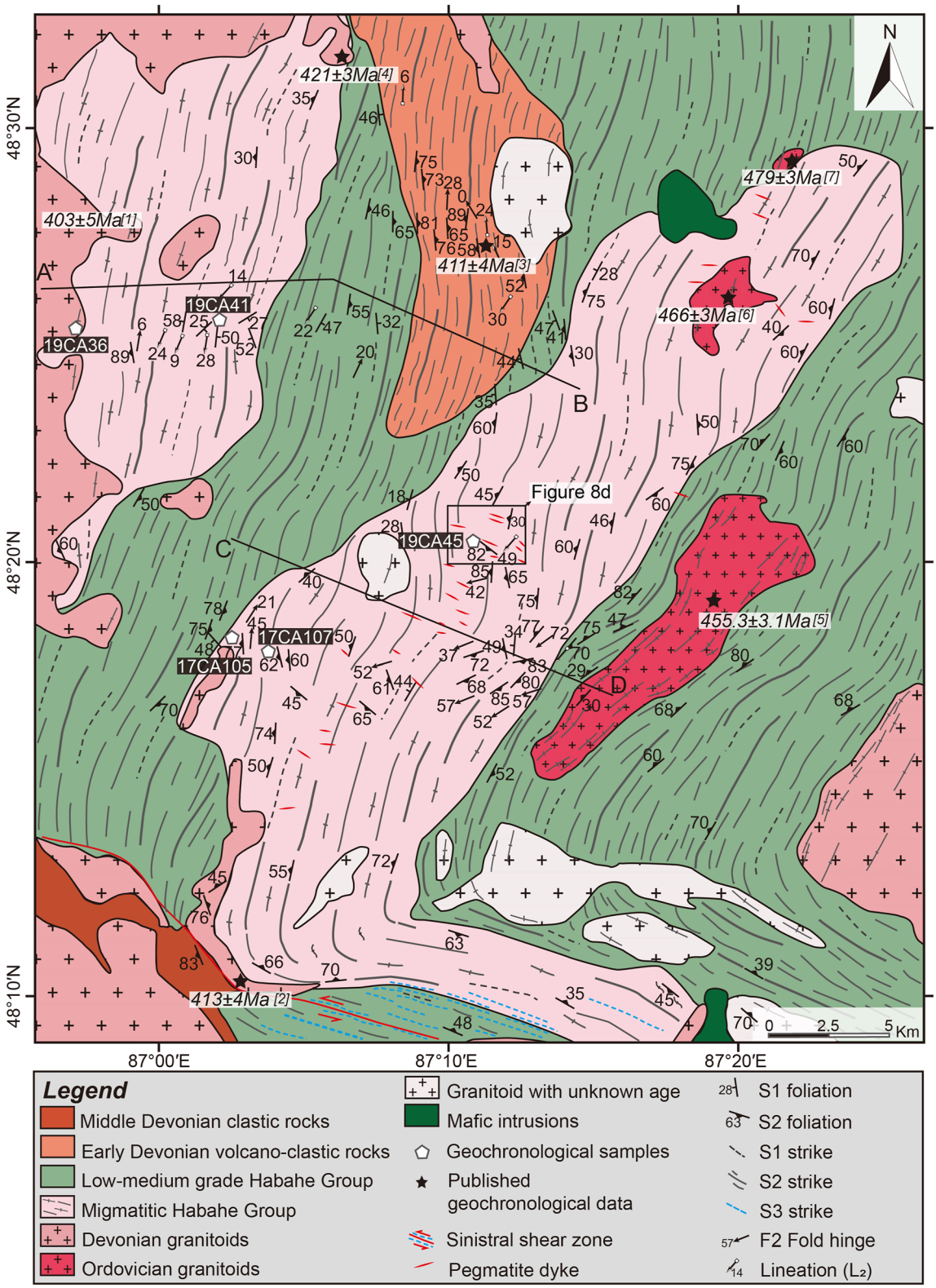

Figure 2. Geological and structural map of the study area (see position in Figure 1c) showing the attitudes of main planar and linear structures. Locations of geological profiles and studied samples as well as published geochronological data are indicated. Sources for published ages: (1) (Tong et al., 2005); (2) (Zeng et al., 2007); (3) (Wang et al., 2011); (4) (Zheng et al., 2016); (5) (Jia Erken·Tu, 2016); (6) (Sun et al., 2009); and (7) (Cai et al., 2011b).

19449194, 2022, 9, Downloaded from https://agupubs.onlinelibrary.wiley.com/doi/10.1029/2021TC007195 by Portail BibCNRS INSU, Wiley Online Library on [06/12/2023]. See the Terms and Conditions (https://onlinelibrary.wiley.com/terms-and-conditions) on Wiley Online Library for rules of use; OA articles are governed by the applicable Creative Commons License

these granitoids crystallized at 405-400 Ma (Cai et al., 2011b; Tong et al., 2005), being slightly older than the reported high-temperature metamorphic age in the region.

Apart from the granitoid intrusions, many meter-scale wide and hundreds of meters to kilometer-long leucogranites and/or pegmatite dykes occur and cross-cut the metamorphosed Habahe Group rocks. These intrusions consist of K-feldspar, quartz, muscovite, and less commonly, garnet and tourmaline. Up to date, these dykes have not been investigated by geochronological and geochemical studies.

3. Structural Descriptions

The metamorphosed Habahe Group can be subdivided into N-S trending migmatitic and non-migmatitic zones. The former consists of variable high-grade gneisses, migmatites and anatectic granites, and the latter is composed of low-grade slates, phyllites, and medium-grade mica gneisses and/or schists (Figure 2). The structurally highest Devonian sequences occur in the northern and southern parts of the study area (Figure 2). In order to characterize the deformational history of the region, detailed structural mapping was conducted along with two nearly E-W-oriented geological transects, perpendicular to the major structural grain. The results are presented in a structural map (Figure 2), interpretative cross-sections, and stereonets (Figure 3). Representative structures are shown in field photographs (Figures 4–8). The structural analysis allowed the definition of three principal deformational episodes (designated D1, D2, and D3) that are described in the following text.

3.1. Structures of the Metamorphosed Habahe Group

In low-grade Habahe Group rocks, the S1 foliation is sometimes parallel to compositional banding interpreted as transposed sedimentary bedding (S0). In medium-grade mica schists, the S1 foliation is defined by the alternation of quartz-rich and mica-rich layers (Figures 4a and 4b). In migmatites, it is defined by lit-par-lit stromatic alternation of quartzo-feldspathic leucosome and biotite-rich melanosome (Figure 5a). Notably, the migmatitic layering in high-grade rocks is in place crosscut by moderately dipping extensional melt-filled shear bands (Figure 5b). No mineral lineation could be identified on the S1 surface.

The S1 foliation in the metamorphic Habahe Group was subsequently variably affected by nearly N-S-trending upright, open to close, F2 folds with wavelengths varying from centimeters to hundreds of meters. The F2 folding is responsible for the rotation of S1 to moderately dipping, or less commonly to vertical attitudes (Figures 4c, 5c, and 5d). As a result, the S1 foliation dips either to the E or W and defines kilometer-scale N-S trending synclines and anticlines, which results in the alternation of migmatitic and non-migmatitic Habahe Group rocks in map view (Figure 2). The rotated S1 foliation bears shallowly N- or S-plunging intersection lineation L_2 (Figures 4e and 5e), parallel to the sub-horizontal F2 fold hinges. In high-strain D2 zones where early S1 foliation was transposed, S2 foliation is parallel to the sub-vertical F2 axial planes (Figure 4d). This is particularly evident in the migmatitic rocks, where new subvertical migmatitic foliation S2 is present (Figure 5d). Less commonly, the S1-parallel leucosomes are continuously connected to axial planar leucosomes truncating the F2 fold hinges (Figure 5f). In places, the compositionally heterogeneous migmatites contain more than 20–40 vol% of granitic leucosomes (Figures 5g and 5h) and commonly show non- or weakly foliated fabric containing numerous cm- to m-scale biotite-rich schollen of stromatic migmatites. These schollen are dismembered to different degrees, and are either shallow-dipping and asymmetrical in F2 fold limbs (Figure 5g) or are parallel to subvertical S2 foliation in the cores of F2 folds (Figure 5h).

The D3 event affected the region heterogeneously and resulted in slight bending of D2 structures by open upright F3 folds in most of the mapping area (see Figure 2). By contrast, in the southernmost part of the studied region, the S2 fabric is rotated into a WNW-ESE-trend, nearly orthogonal to its original N-S trend, defining a map-scale mega-F3 fold in the region (Figure 2). Here, a spaced greenschist-facies cleavage S3 is parallel to the short limbs of F3 parasitic folds (Figure 2). Notably, a mylonitic zone is developed parallel to S3 along with the contact between the Habahe Group and the Devonian clastic sequence in the south. This mylonitic zone is several hundred meters wide and characterized by steeply dipping mylonitic foliation (Figure 4f) associated with a sinistral sense of shear criteria and a subhorizontal stretching lineation L_3 (Figures 4g and 4h) (Wang et al., 2021; Zhang et al., 2015).

19449194, 2022, 9, Downloaded from https://agupubs.onlinelibrary.wiley.com/doi/10.1029/2021TC007195 by Portail BibCNRS INSU, Wiley Online Library on [06/12/2023]. See the Terms and Conditions (https://onlinelibrary.wiley.com/terms-and-conditions) on Wiley Online Library for rules of use; OA articles are governed by the applicable Creative Commons License

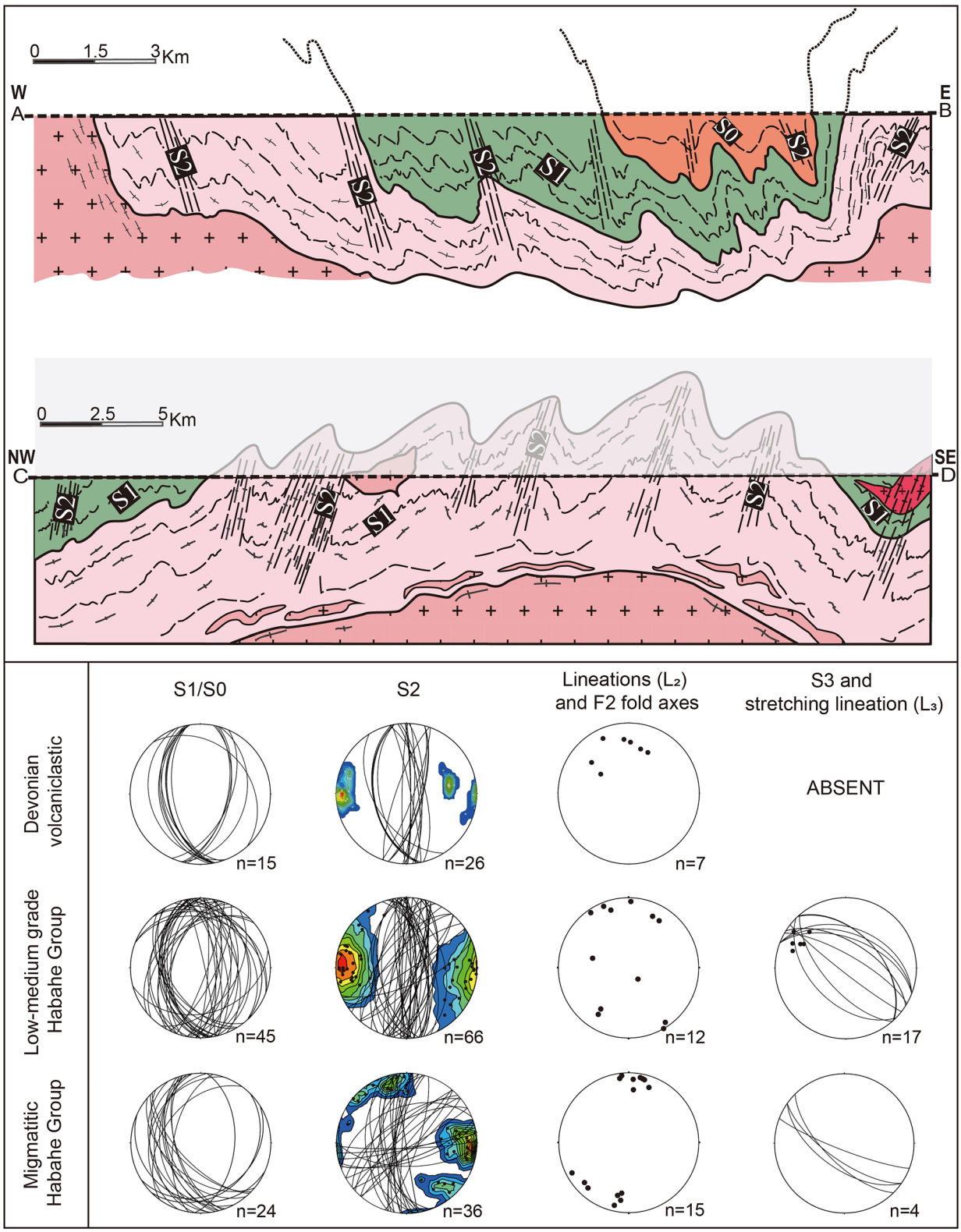

Figure 3. Interpretative cross-sections and stereoplots (lower hemisphere, equal area projections) show the deformational features and orientations of the major structural elements of different units. Note that vertical axes of the cross-sections are not scaled. For legend see Figure 2.

19449194, 2022, 9, Downloaded from https://agupubs.onlinelibrary.wiley.com/doi/10.1029/2021TC007195 by Portail BibCNRS INSU, Wiley Online Library on [06/12/2023]. See the Terms and Conditions (https://onlinelibrary.wiley.com/terms-and-conditions) on Wiley Online Library for rules of use; OA articles are governed by the applicable Creative Commons License

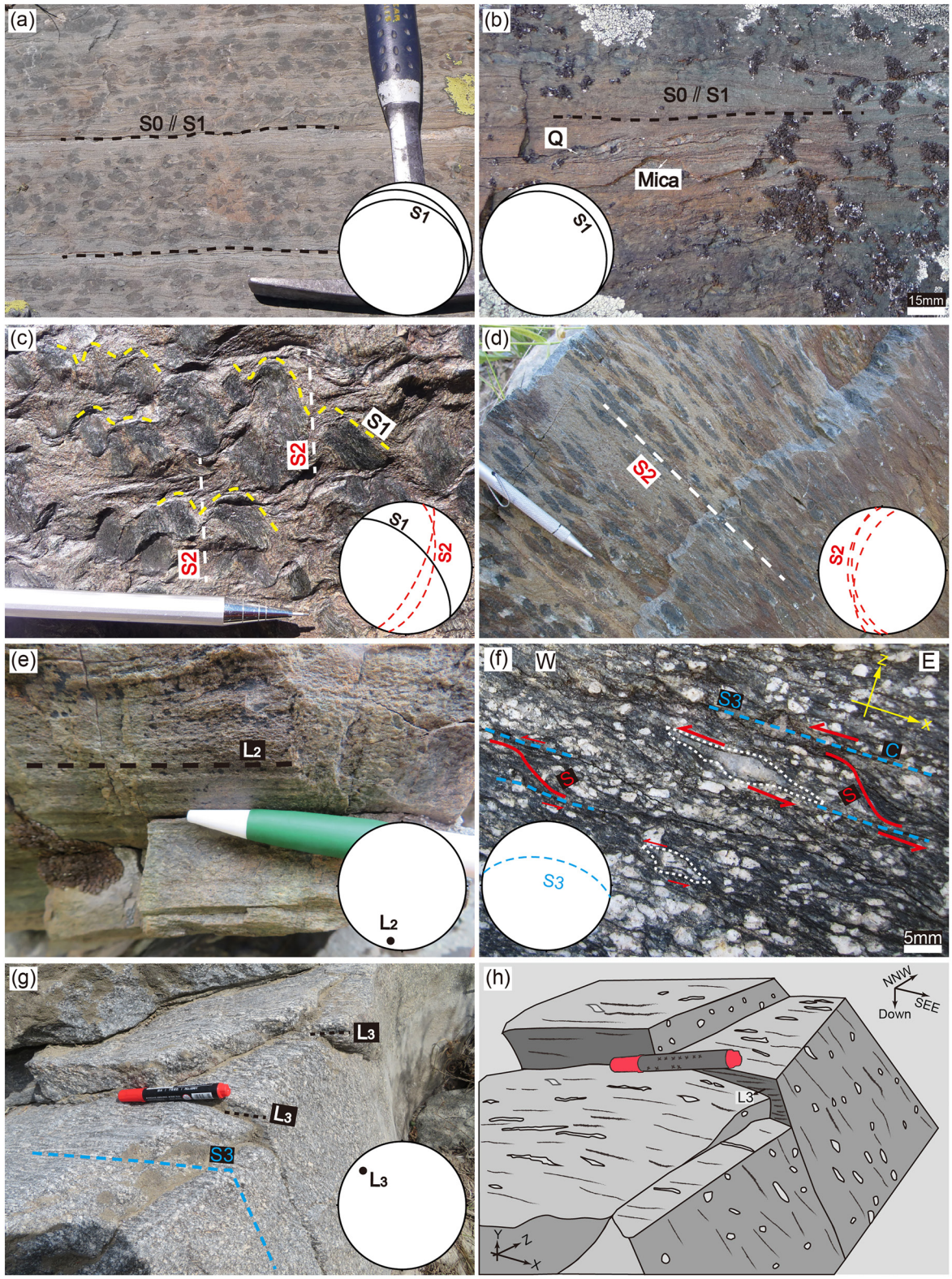

Figure 4.

19449194, 2022, 9, Downloaded from https://agupubs.onlinelibrary.wiley.com/doi/10.1029/2021TC007195 by Portail BibCNRS INSU, Wiley Online Library on [06/12/2023]. See the Terms and Conditions (https://onlinelibrary.wiley.com/terms-and-conditions) on Wiley Online Library for rules of use; OA articles are governed by the applicable Creative Commons License

19449194, 2022, 9, Downloaded from https://agupubs.onlinelibrary.wiley.com/doi/10.1029/2021TC007195 by Portail BibCNRS INSU, Wiley Online Library on [06/12/2023]. See the Terms and Conditions (https://onlinelibrary.wiley.com/terms-and-conditions) on Wiley Online Library for rules of use; OA articles are governed by the applicable Creative Commons License

3.2. Structures of the Devonian Sedimentary Succession

This study mainly focuses on the structures of the Devonian volcano-clastic succession in the northern part of the study area, since those of the southern counterparts have been already documented in previous studies (Jiang et al., 2015; Wang et al., 2018; Zhang et al., 2015). These studies documented that the sedimentary bedding (S0) was folded into a series of NW-SE upright folds with a spaced axial planar cleavage (S2) defined by the preferred orientations of sericite, chlorite, and biotite. Similarly, the northern exposures of the Devonian succession are located in the core of a regional F2 synform (Figures 2 and 3). This succession is characterized by a strong, roughly N-S-striking S2 schistosity. Although the bulk succession was extensively affected by D2 deformation, the bedding (S0, Figure 6a) and sedimentary texture (Figure 6b) are still preserved, and no clues of S1 metamorphic fabric have yet been observed. The N-S striking S2 foliation bears shallowly plunging intersection lineation L_2 (Figures 6c–6e), attesting to the originally flat attitudes of pre-folding S0. The D2 structures were only slightly bent by D3 (Figure 2).

3.3. Structures of Ordovician and Devonian Granitoids and Leucogranite Dykes

The Ordovician granitoid intrusions are generally strongly deformed and show a significant solid-state gneissosity parallel to S2 defined by the shape-preferred orientation of recrystallized feldspar, quartz, and biotite. Preservation of an early fabric marked by the alignment of mica and feldspar crystals can be observed in some places (Figure 7a). By contrast, the Devonian granitoids show variable deformational features according to the degree of metamorphism of the host rock. The granitoids intruding non-migmatitic low-to-medium-grade metamorphosed Habahe Group rocks show a strong solid-state S2 foliation defined by parallel planar arrangement of recrystallized feldspars and micas (Figure 7b), similar to the S2 foliation developed in the Ordovician granitoids. In contrast, granitoids emplaced within the Habahe Group migmatites commonly show an important magmatic flow fabric defined by preferred orientation of restitic schlieren and the alignment of feldspars, defining a flat linear fabric in the rocks (Figure 7c). In addition, well-oriented euhedral muscovite, and biotite locally define a strong magmatic foliation in the granitoids, which is parallel to the S2 foliation in the schollens of host rock migmatites (Figure 7d).

Leucogranite and pegmatite dikes are also commonly emplaced along the F2 axial planes or show continuities with veins in S1 that were further folded by minor F2 folds (Figures 8a and 8b). Other veins are almost undeformed and crosscut the F2 hinges and regional S2 foliation in a nearly perpendicular orientation (Figures 8c and 8d).

3.4. Deformation-Metamorphism Relationships

Deformation-metamorphism relationships are examined in order to link the growth of metamorphic minerals with the succession of macroscopic fabrics described above. In this section, only petrostructural characteristics of the metamorphosed Habahe Group rocks are summarized as the Devonian volcano-clastic rocks were deformed at low-grade metamorphic conditions and do not show an informative relationship between crystal growth and deformation. In the following paragraphs, the petrostructural features of deep crustal migmatites and mid- to shallow crustal schists and phyllites are described separately and a summary of crystallization-deformation relations is provided thereafter.

3.4.1. Migmatitic Domains of the Habahe Group

Microstructural observations indicate that the S1 foliation is usually defined by shape preferred orientation of biotite and sillimanite (Figures 9a–9c). Garnet porphyroblasts up to 2–3 mm in size contain inclusion trails of aligned ilmenite and quartz, which are continuous with the external S1 foliation (Figure 9a). Hypidiomorphic K-feldspar grains are also aligned parallel to the migmatitic S1 foliation. Importantly, staurolite relics appear

Figure 4. Representative field photographs showing the main structures of the low-medium-grade Habahe Group domains: (a) S1 foliation is defined by alternation of quartz-rich and mica-rich layers; (b) Flat S1 foliation parallel to compositional bedding S0; (c) S1 foliation reworked by upright open F2 folds; (d) Newly formed penetrative S2 foliation; (e) Subhorizontal intersection lineation L_2 indicative of an originally subhorizontal attitude of S1 foliation prior to F2 folding; and (f) Mylonitic S3 foliation in the metamorphosed Habahe Group from the southern part of the study area. Note σ-type feldspar and quartz porphyroclasts and S-C fabrics indicative of a sinistral sense of shear (g–h) Highly deformed granite near the shear zone in the south. Note S3 foliation bears horizontal stretching lineation L_3. Distinct deformation features on XY and YZ planes of the D3 strain ellipsoid, and horizontal stretching linear fabric are also indicated in the sketch.

10.1029/2021TC007195

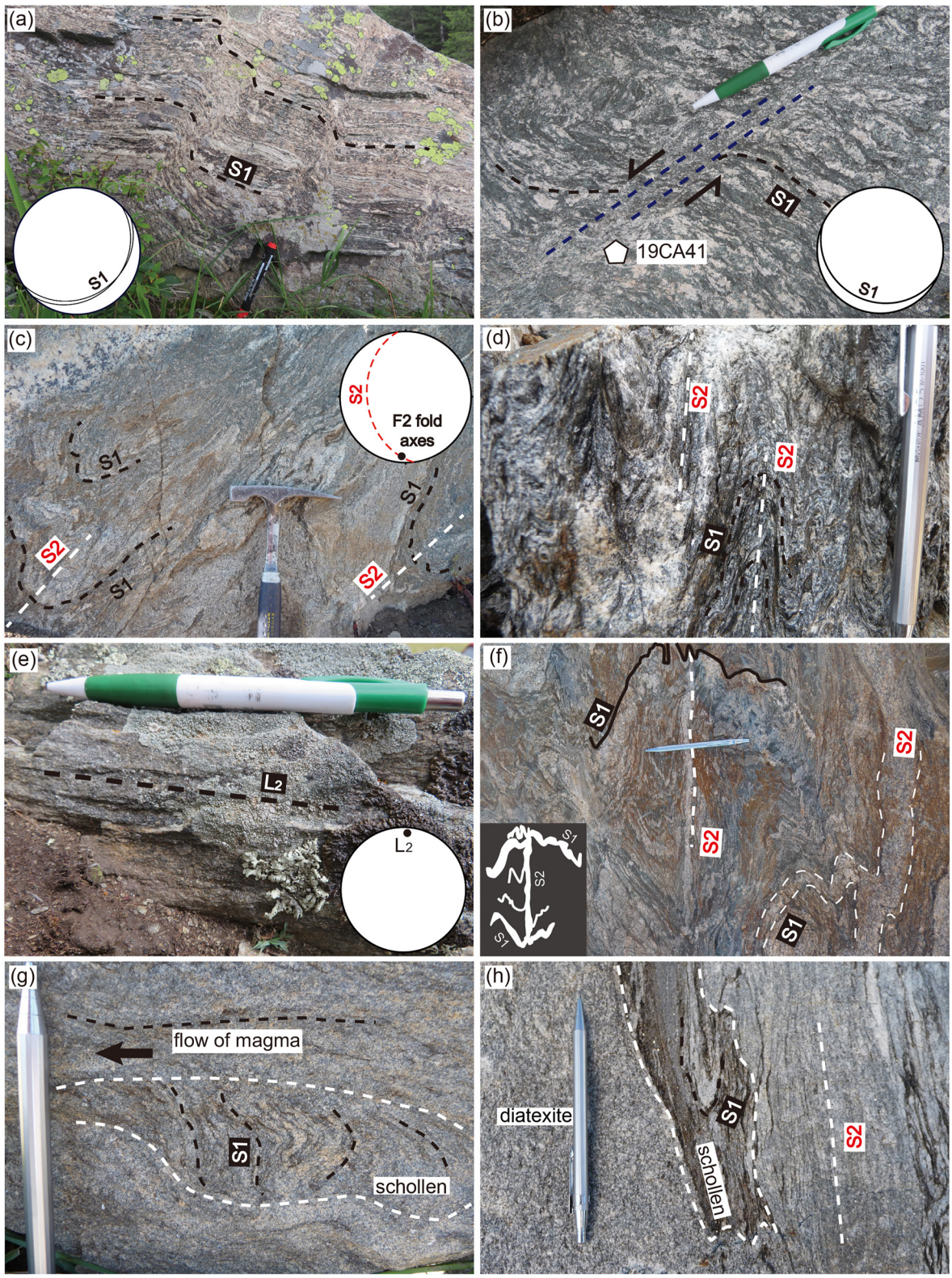

Figure 5. Representative field photographs showing the main structures of the migmatitic domains of the metamorphosed Habahe Group: (a) Subhorizontal S1 defined by alternating quartzo-feldspathic leucosome and biotite-rich melanosome; (b) Subhorizontal migmatitic fabric S1 associated with extensional shear bands; (c) S1 foliation folded by open F2 upright fold; (d) S1 foliation folded by close F2 folds and transposed by S2 foliation in places; (e) Subhorizontal intersection lineation L_2; (f) S1-parallel leucosomes in continuity with the axial planar leucosomes of F2 folds; (g) Shallow-dipping schollen in the limbs of F2 are oblique to magma flow; and (h) Schollen in massive diatexite.

19449194, 2022, 9, Downloaded from https://agupubs.onlinelibrary.wiley.com/doi/10.1029/2021TC007195 by Portail BibCNRS INSU, Wiley Online Library on [06/12/2023]. See the Terms and Conditions (https://onlinelibrary.wiley.com/terms-and-conditions) on Wiley Online Library for rules of use; OA articles are governed by the applicable Creative Commons License

10.1029/2021TC007195

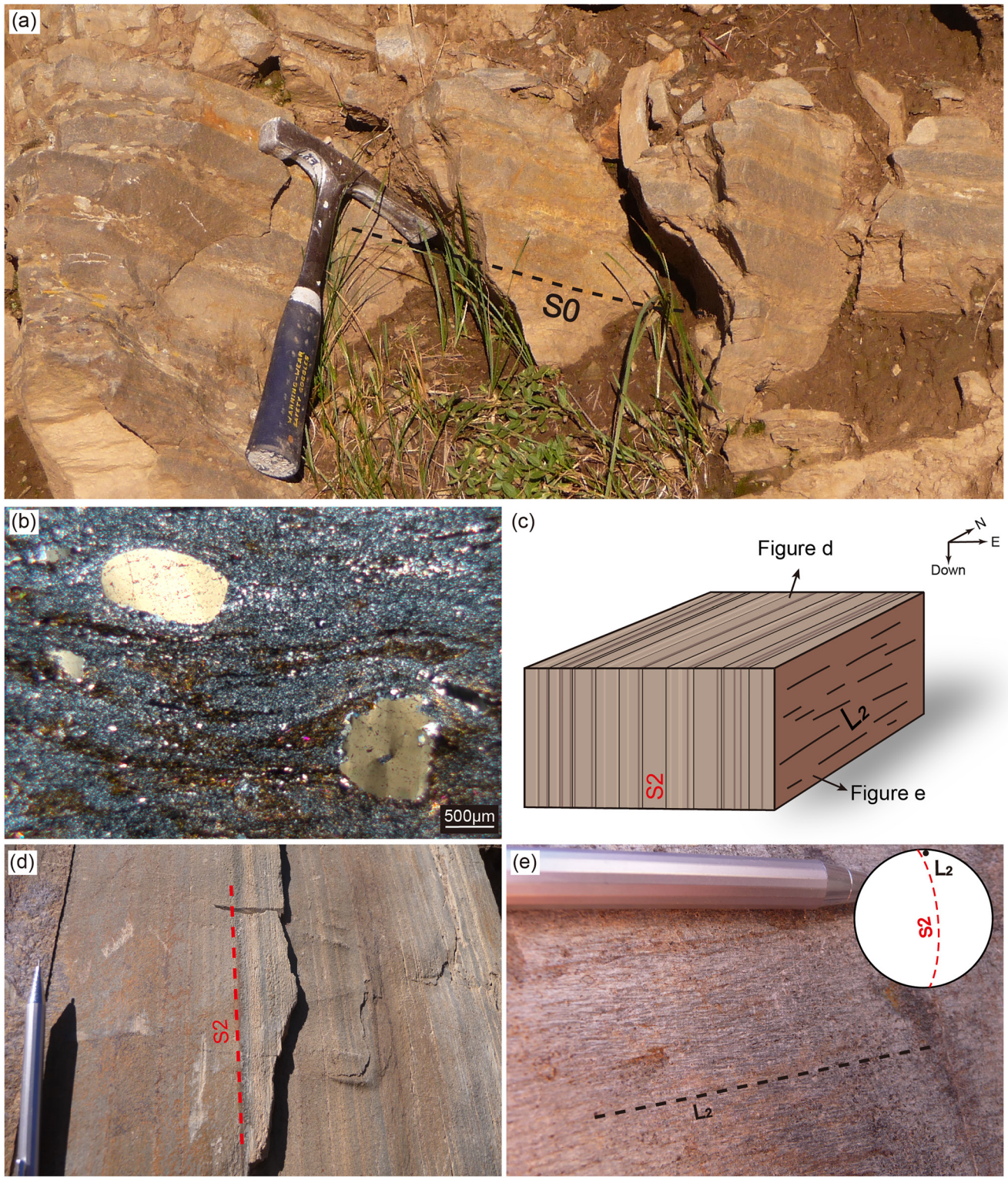

Figure 6. Representative photographs showing the main structures of the Devonian volcano-clastic sequence: (a) Sedimentary bedding S0; (b) Photomicrograph showing the texture of volcano-clastic rock; (c) Schematic diagram showing S2 foliation and intersection lineation L_2; (d) Newly formed penetrative S2 foliation; and (e) Subhorizontal intersection lineation L_2 in the Devonian volcano-clastic sequence.

19449194, 2022, 9, Downloaded from https://agupubs.onlinelibrary.wiley.com/doi/10.1029/2021TC007195 by Portail BibCNRS INSU, Wiley Online Library on [06/12/2023]. See the Terms and Conditions (https://onlinelibrary.wiley.com/terms-and-conditions) on Wiley Online Library for rules of use; OA articles are governed by the applicable Creative Commons License

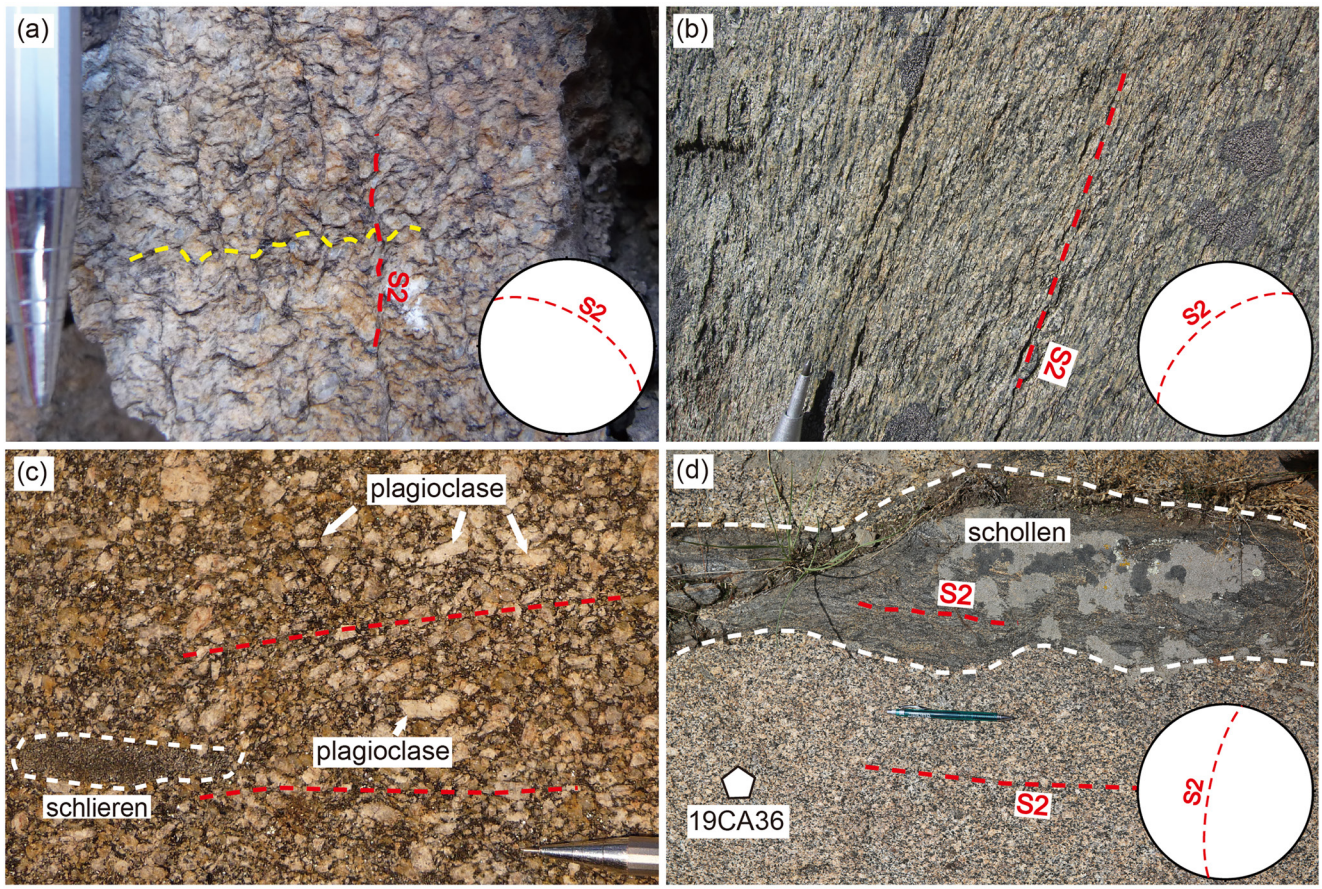

Figure 7. Representative structures of granitoids in the study area. (a) Preservation of an earlier fabric in the Ordovician granitoid, which was further reworked by D2 event; (b) Devonian granitoid intruded into non-migmatitic Habahe Group with a solid-state S2 foliation; (c) Devonian granite in migmatitic Habahe Group domain with an N-S trending subvertical magmatic S2 defined by preferred orientation of feldspar crystals and biotite-rich schlieren; and (d) Schollen with internal structures parallel to magmatic S2 foliation of the host granite.

locally in the migmatitic S1 foliation. While the S1 foliation is well preserved in low-strain domains affected by F2 folding (Figures 9a and 9b), its counterpart is entirely transposed by steep penetrative S2 foliation in high-strain zones (Figures 9d and 9e). In the latter case, the S1-parallel leucosomes composed of coarse-grained and euhedral K-feldspar and plagioclase crystals are in continuity with the axial planar leucosomes of F2 folds. Less commonly, euhedral muscovite and plagioclase crystals show preferred orientation, defining a strong magmatic S2 fabric (Figure 9d). Anhedral andalusite and cordierite porphyroblasts are generally aligned parallel to the newly formed S2 foliation (Figures 9e–9g). In some places, these porphyroblasts overgrow fibrolitic sillimanite (Figures 9d and 9h) and fragments of staurolite (Figure 9f).

3.4.2. Habahe Group Mica Schists and Phyllites

The flat S1 foliation is defined by alternations of millimeter to centimeter thick phyllosilicates-rich and quartz-rich layers in the relatively lower-grade phyllites and slates and by alternating plagioclase-quartz-rich and biotite-rich layers in the relatively higher-grade mica schists. A striking feature is the common development of cordierite porphyroblasts (Figure 10a), in particular in the northern part of the studied area. Cordierite porphyroblasts up to several centimeters across contain straight inclusion trails showing continuity with the external S1 foliation and sometimes poorly defined strain shadows (Figure 10b). Mineral inclusions in the cordierites have the same compositions as matrix minerals, but the latter are coarser. During D2 folding, the S1 foliation was rotated together with cordierite porphyroblasts. While in the low-strain D2 domains, the straight mineral inclusion trails are still connected with the external curved S1 foliation (Figure 10b), in the high strain D2 zones the mineral trails are usually oblique to or even perpendicular to the external S2 foliation (Figure 10c). Except for local replacement of cordierite by quartz and sericite pseudomorphs (Figures 10a and 10c) and recrystallization of micas along the

19449194, 2022, 9, Downloaded from https://agupubs.onlinelibrary.wiley.com/doi/10.1029/2021TC007195 by Portail BibCNRS INSU, Wiley Online Library on [06/12/2023]. See the Terms and Conditions (https://onlinelibrary.wiley.com/terms-and-conditions) on Wiley Online Library for rules of use; OA articles are governed by the applicable Creative Commons License

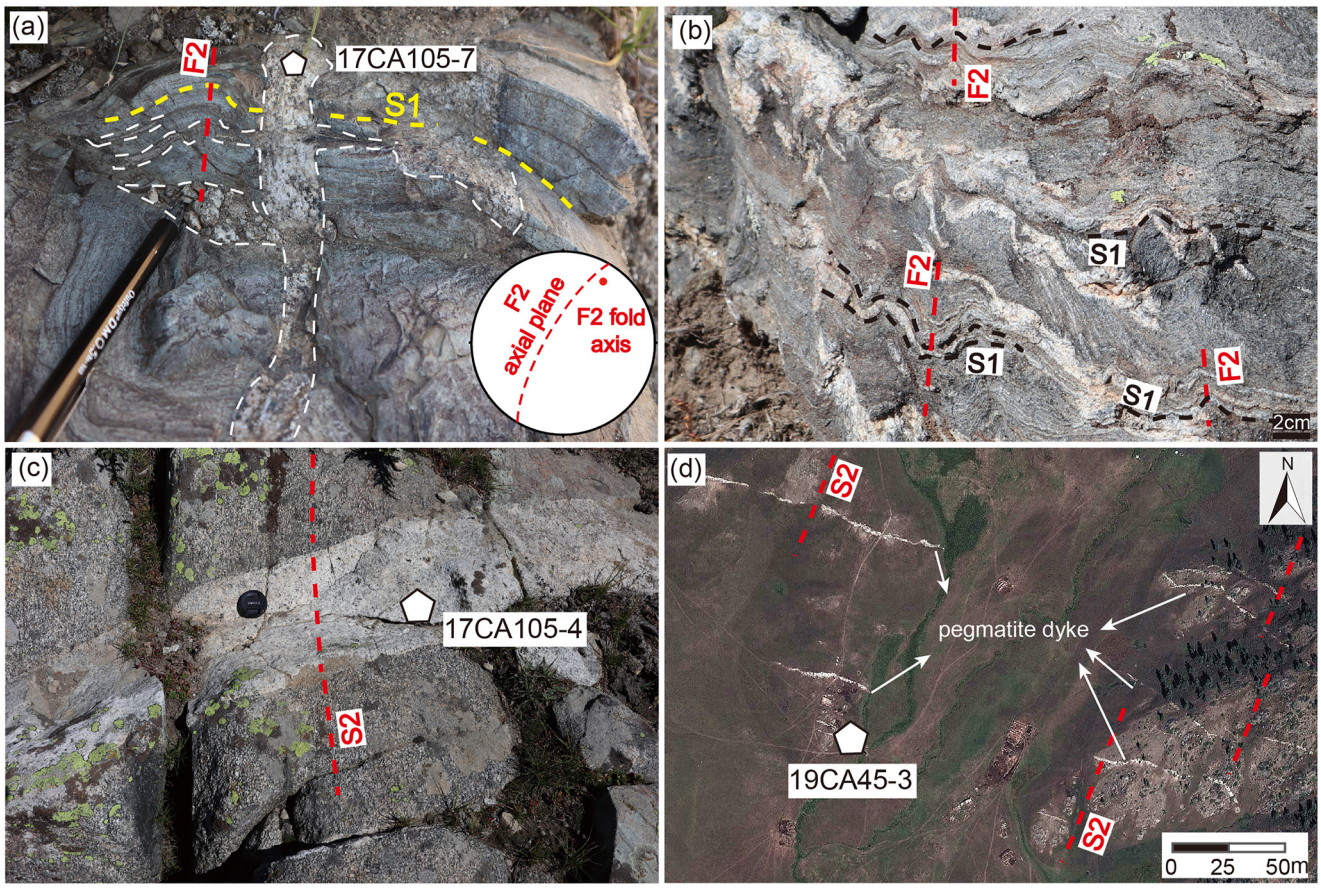

Figure 8. Representative structures of leucogranite and pegmatite dykes in the study area. (a) A leucogranite vein emplaced as a structure-controlled intrusion parallel to the axial plane of F2 folds in the low-medium-grade Habahe Group domains; (b) Leucogranite veins emplaced parallel to the S1 foliation in the un-molten Habahe Group domain folded by F2. Note that (a, b) are from the same outcrop; (c) Leucogranitic dyke (sample 17CA105-4) emplaced nearly perpendicular to regional S2 foliation; and (d) Aerial photograph showing nearly W-E-orientated pegmatites emplaced perpendicular to the nearly N-S-trending regional S2.

F2 axial planes, the mineral assemblage constituting the S1 foliation remained well-preserved after D2. In some places, quartz + sericite + chlorite aggregate formed pseudomorphs after staurolite (Figure 10d). These pseudomorphs also preserved straight inclusion trails that are in continuity with the external S1 foliation.

3.4.3. Summary and Interpretations

3.4.3.1. Index Minerals Related to D1 and D2

The index minerals garnet, sillimanite, and K-feldspar crystals are found within the migmatitic S1 foliation where they are either preferably aligned along the S1 or contain inclusion trails that are in continuity with the external S1 foliation (Figures 9a, 9b, and 11a). These features suggest their syntectonic growth with respect to the migmatitic S1 foliation (Figure 11b) and support the interpretation that S1 developed under at least upper amphibolite-facies. In the low-to-medium grade metamorphosed Habahe Group rocks, S1 was overgrown by cordierite porphyroblasts during D1 deformation (Figures 10b and 11a) and the deformation persisted even after the crystal growth of the cordierite (Figure 11b).

During the D2 event, a migmatitic S2 foliation was developed in the high-grade Habahe Group rocks, associated with shape preferred orientations of cordierite and andalusite porphyroblasts, some of which contain S1 sillimanite (Figures 9e, 9g, 9h, and 11a). These features suggest that their growth postdates sillimanite and is probably synchronous with S2 (Figure 11b). In the low-medium grade Habahe Group rocks, the bulk cordierite-bearing S1 assemblage remained (meta) stable except for the possible recrystallization of biotite and muscovite along S2 axial planes (Figures 10c and 11).

19449194, 2022, 9, Downloaded from https://agupubs.onlinelibrary.wiley.com/doi/10.1029/2021TC007195 by Portail BibCNRS INSU, Wiley Online Library on [06/12/2023]. See the Terms and Conditions (https://onlinelibrary.wiley.com/terms-and-conditions) on Wiley Online Library for rules of use; OA articles are governed by the applicable Creative Commons License

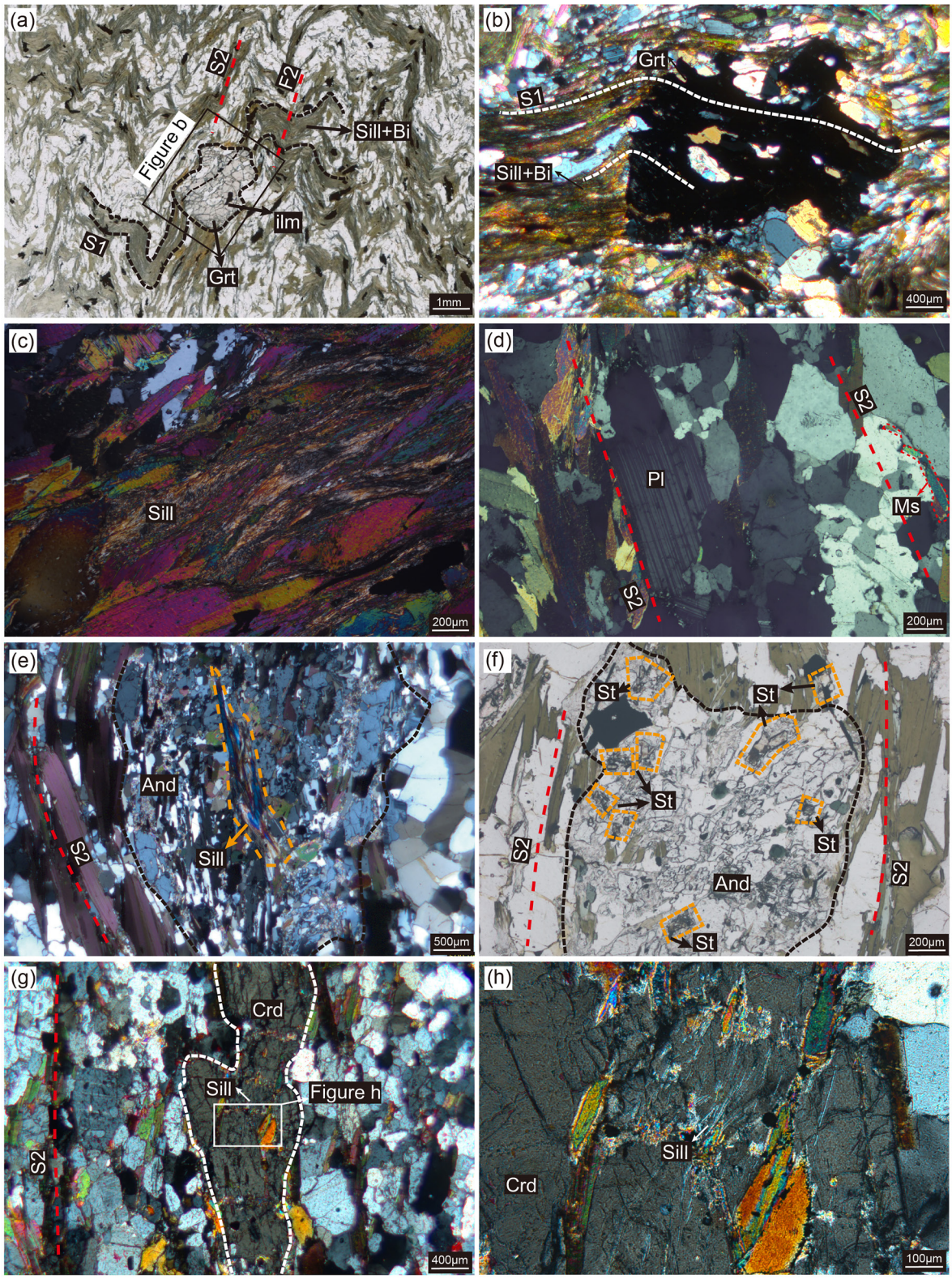

Figure 9.

19449194, 2022, 9, Downloaded from https://agupubs.onlinelibrary.wiley.com/doi/10.1029/2021TC007195 by Portail BibCNRS INSU, Wiley Online Library on [06/12/2023]. See the Terms and Conditions (https://onlinelibrary.wiley.com/terms-and-conditions) on Wiley Online Library for rules of use; OA articles are governed by the applicable Creative Commons License

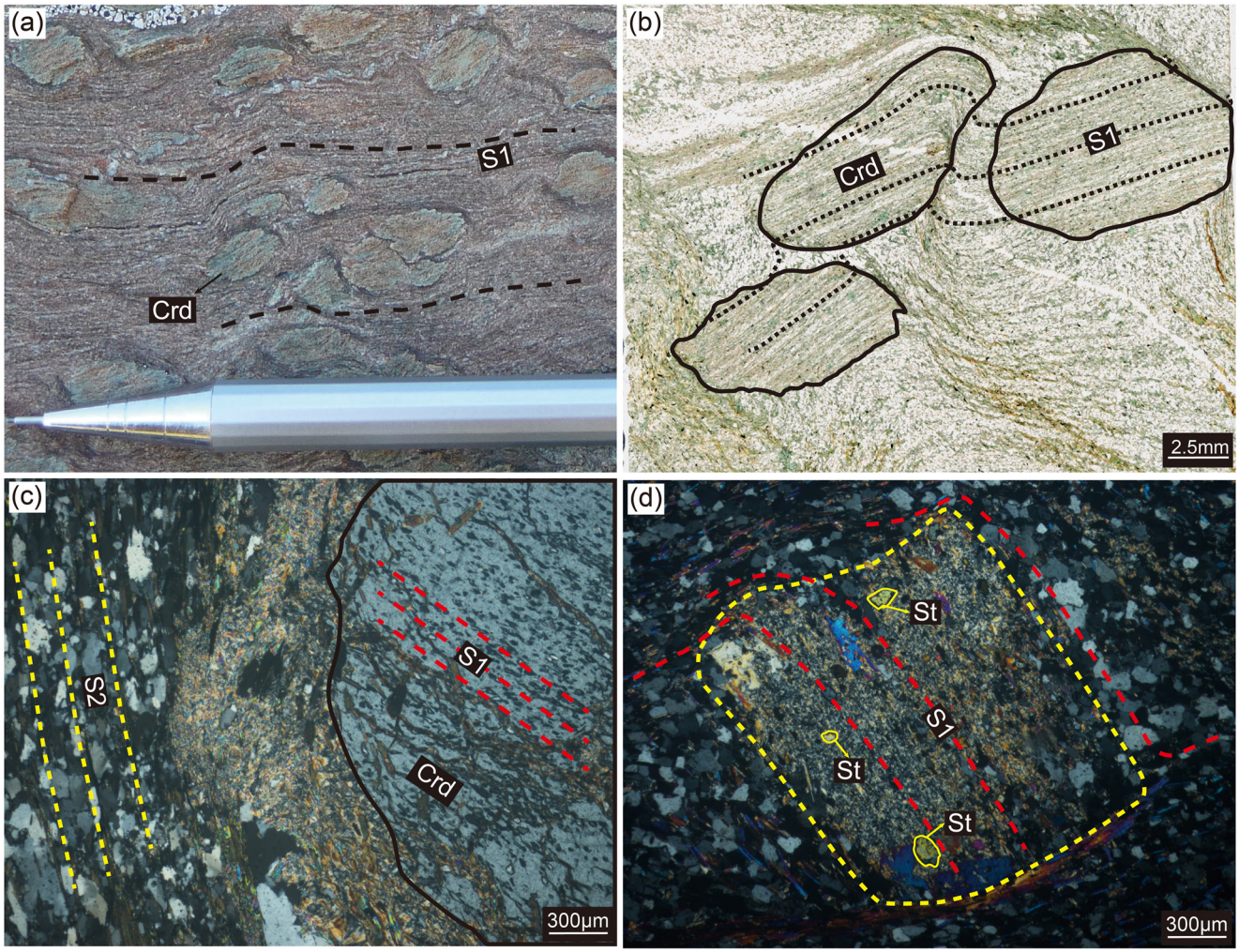

Figure 10. Representative photomicrographs of the Habahe Group mica schists and phyllites. (a) Field photograph shows the growth of cordierite porphyroblasts in the flat S1 foliation; (b) Cordierite poikiloblasts (outlined by solid lines) containing inclusion trails of biotite, continuous with the external S1 foliation (delineated by dashed lines); (c) A cordierite poikiloblast containing straight inclusion trails that are oblique to the external S2 foliation; and (d) Staurolite is pseudomorphed by an aggregate of sericite and quartz. Note the pseudomorph preserves staurolite relics and inclusions trails continuous with the external foliation. Mineral abbreviations are: Crd, cordierite and St, staurolite.

3.4.3.2. Staurolite Relics: Indication of an Early Barrovian-type Fabric?

Staurolite relics are preserved in both migmatitic and low-medium grade Habahe Group rocks but their geometrical relations to the identified metamorphic fabric are not clear. Nevertheless, S1 foliation associated with garnet, staurolite, and kyanite was documented in medium-grade Habahe Group rocks located in the southern limb of the mega-F3 fold and was interpreted to record a regional Barrovian-type fabric (Jiang et al., 2015). Importantly, garnet porphyroblasts containing straight staurolite, and kyanite inclusion trails and laying within a sillimanite-K-feldspar-bearing high temperature fabric were also observed in the migmatite domain equivalent to that examined in this study (e.g., Jiang et al., 2015). Later on, in the Aletai region, some 100 km to the east, Jiang et al. (2019, 2022) observed parallelism between internal foliation in staurolite and garnet porphyroblast and sillimanite-bearing external foliation in the matrix. There, the growth of the sillimanite occurred at the expense

Figure 9. Photomicrographs of the migmatitic Habahe Group domain (a, b) Folded S1 foliation defined by preferred orientation of biotite, sillimanite, and ilmenite. Note inclusion trails in the garnet are continuous with the external S1 foliation; (c) Migmatitic S1 foliation containing aligned sillimanite; (d) Euhedral muscovite and plagioclase crystals show preferred orientation, defining a strong S2 magmatic fabric; (e) Growth of andalusite in F2 planar leucosomes. Note that andalusite porphyroblasts overgrow the S1 index mineral sillimanite; (f) Staurolite relics locally preserved in the migmatitic Habahe Group domains; and (g–h) Cordierite porphyroblasts in the F2 planar leucosomes containing S1 sillimanite inclusions. Mineral abbreviations are: Sill, sillimanite; Grt, garnet; Crd, cordierite; And, andalusite; and St, staurolite.

19449194, 2022, 9, Downloaded from https://agupubs.onlinelibrary.wiley.com/doi/10.1029/2021TC007195 by Portail BibCNRS INSU, Wiley Online Library on [06/12/2023]. See the Terms and Conditions (https://onlinelibrary.wiley.com/terms-and-conditions) on Wiley Online Library for rules of use; OA articles are governed by the applicable Creative Commons License

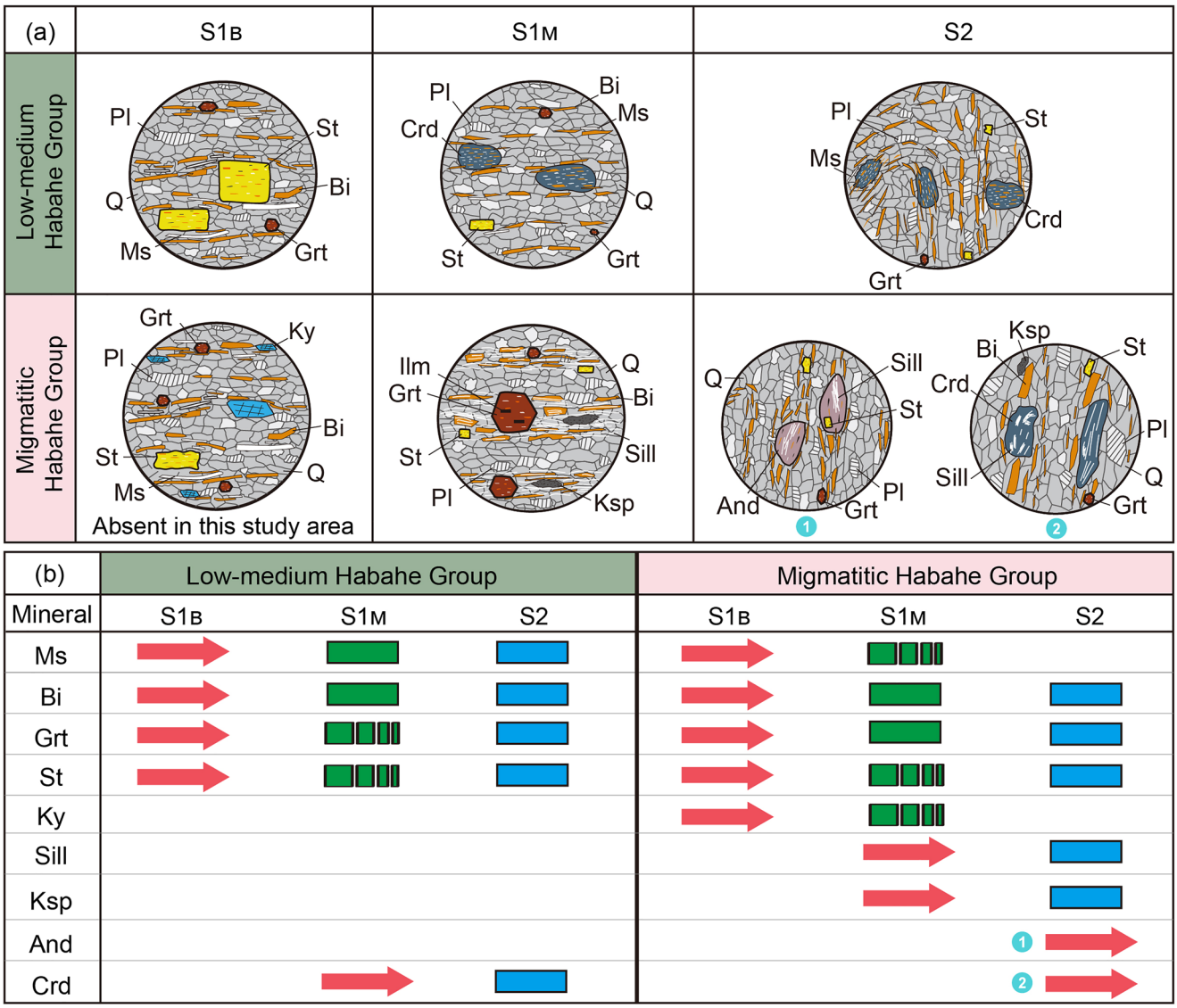

Figure 11. (a) Interpretative sketches of mineral successions associated with distinct deformation episodes. The $S1_B$ is mainly inferred from previous studies of Jiang et al. (2015), Jiang et al. (2019), and Jiang et al. (2022); (b) Schematic deformation–crystallization relationships of index minerals in the low-medium and high-grade Habahe Group rocks. The red arrow indicates growth of minerals, the green solid line reflects their stability, green dashed line means decomposition, and blue solid line represents metastable state.

of the staurolite. In addition, the sillimanite-bearing external foliation was also parallel to subhorizontal migmatite layering at the deeper crustal level. In these regions, all these fabrics share the same D2 and D3 deformation overprints. Therefore, the foliation preserved in Barrovian minerals has been considered to represent an early $S1_B$ foliation and the sillimanite-bearing fabric and migmatitic one as late foliation labeled as $S1_M$. Accordingly, the related deformation episodes during the D1 event have been termed the $D1_B$ and subsequent $D1_M$. In this study, the high-temperature/low-pressure garnet-sillimanite-K-feldspar-bearing foliation in the deep crustal level and cordierite-bearing foliation in the shallower crustal levels, both contain staurolite and garnet relics. The former fabric can be considered as the counterparts of $S1_M$ while the presence of garnet and staurolite relics suggests poor preservation of an $S1_B$ Barrovian-type fabric. In contrast to the Aletai area, the $S1_B$ fabric in the mapping area was probably completely transposed by $S1_M$ foliation (Figure 11).

19449194, 2022, 9, Downloaded from https://agupubs.onlinelibrary.wiley.com/doi/10.1029/2021TC007195 by Portail BibCNRS INSU, Wiley Online Library on [06/12/2023]. See the Terms and Conditions (https://onlinelibrary.wiley.com/terms-and-conditions) on Wiley Online Library for rules of use; OA articles are governed by the applicable Creative Commons License

19449194, 2022, 9, Downloaded from https://agupubs.onlinelibrary.wiley.com/doi/10.1029/2021TC007195 by Portail BibCNRS INSU, Wiley Online Library on [06/12/2023]. See the Terms and Conditions (https://onlinelibrary.wiley.com/terms-and-conditions) on Wiley Online Library for rules of use; OA articles are governed by the applicable Creative Commons License

4. U-Pb Zircon and Monazite Geochronology

4.1. Sampling Strategy

In order to provide critical geochronological constraints on the individual fabrics, seven samples were collected from key lithological units for zircon and monazite U-Pb dating (sample locations are shown in Figure 2), including two zircon samples (19CA36 and 17CA105-7) and five monazite samples (17CA107, 17CA105-4, 19CA41, 19CA45-1, and 19CA45-3).

The zircon sample 19CA36 was collected from a two-mica granite characterized by a strong N-S trending steep magmatic foliation, marked by the shape-preferred orientation of euhedral feldspar, muscovite, and/or alignment of restitic schlieren (Figure 7d) parallel to S2 foliation of the host rock. Another zircon sample 17CA105-7 was collected from a leucogranite vein parallel to the axial plane of F2 folds (Figure 8a), as a typical structure-controlled intrusion. The leucogranite vein shows continuity with leucosomes emplaced along the S1 foliation and affected by the F2 fold. The above structural and petrological features suggest both the granite and leucogranite veins were probably emplaced during ongoing D2 deformation.

Monazite samples 19CA41 and 17CA107 were collected from migmatites that show the subhorizontal stromatic S1 foliation associated with extensional shear bands (Figure 5b). These samples have the potential to date the timing of formation of the S1 fabric. In contrast, another migmatitic gneiss sample 19CA45-1 shows prominent S2 foliation and likely provides the age constraints of the D2 event.

Monazite samples 17CA105-4 and 19CA45-3 represent a weakly sdeformed tourmaline-garnet-bearing leucogranite dyke (Figure 8c) and a pegmatite dyke (Figure 8d), respectively. Both intruded perpendicular to the S2 foliation. The orientation of pegmatite dykes perpendicular to the XY plane of the D2 strain ellipsoid (S2 cleavage) indicates that they were emplaced as tensional gashes parallel to the principal compressive stress (Mode I fractures) (Fossen, 2010). These dykes are therefore considered to be syn- or late-tectonic with respect to the D2 event.

4.2. Analytical Methods

Zircon and monazite grains were separated after rock crushing using conventional heavy liquid and magnetic properties and then selected under a binocular microscope. These grains were mounted in epoxy resin and polished to approximately one-third of their thickness. The internal zircon structures were imaged using cathodoluminescence (CL) detector and a scanning electron microscope (JSM-IT100) connected to a GATAN MINICL system at Wuhan Sample Solution Analytical Technology (WSAT) Co., Ltd., Wuhan, China. Monazite grains were imaged by backscattered electrons (BSE) using the same microprobe instrument. These images were used to study the size, morphology, and internal structure of zircon and/or monazite grains, which were further taken as a guide for the selection of suitable portions for U-Pb dating.

U-Pb dating of zircon and monazite were analyzed by LA-ICP-MS at the WSAT Co., Ltd. U-Pb dating of zircon samples was conducted by a COMPexPro 102 ArF excimer laser and a MicroLas optical system coupled with an Agilent 7700e ICP-MS. Detailed operating conditions for the laser ablation system and the ICP-MS instrument and data reduction were as described by Zong et al. (2017). Most analyses were performed with a beam diameter and frequency of 32 μm and 5 Hz. GJ-1 standard zircon was also determined for monitoring the accuracy of U-Pb dating. Zircon 91500 (ca. 1,065 Ma, Wiedenbeck et al., 1995) was used as an external standard for U-Pb dating calibration. U-Pb dating of monazite samples was performed using the same operating processes and instruments. In this work, the spot size and frequency of the laser were set to 16 μm and 2 Hz, respectively. Monazite standard 44069 (ca. 425 Ma, Aleinikoff et al., 2006) was used as an external standard for U-Pb dating. Monazite standard Trebilcock (ca. 275 Ma, Tomascak et al., 1996) was used as a secondary standard to assess the accuracy of analyses. Each analysis of zircon/monazite was performed using a background acquisition of approximately 25 s followed by 65 s of data acquisition.

An Excel-based software ICPMSDataCal (Liu et al., 2008) was used to process offline selection and integration of background and analyzed signals, time-drift correction, and quantitative calibration for the U-Pb dating of zircon and monazite. Concordia diagrams and weighted mean calculations for all samples were made using Isoplot (version 3.0, Ludwig, 2003). For both zircon and monazite U-Pb dating, uncertainties on single analyses

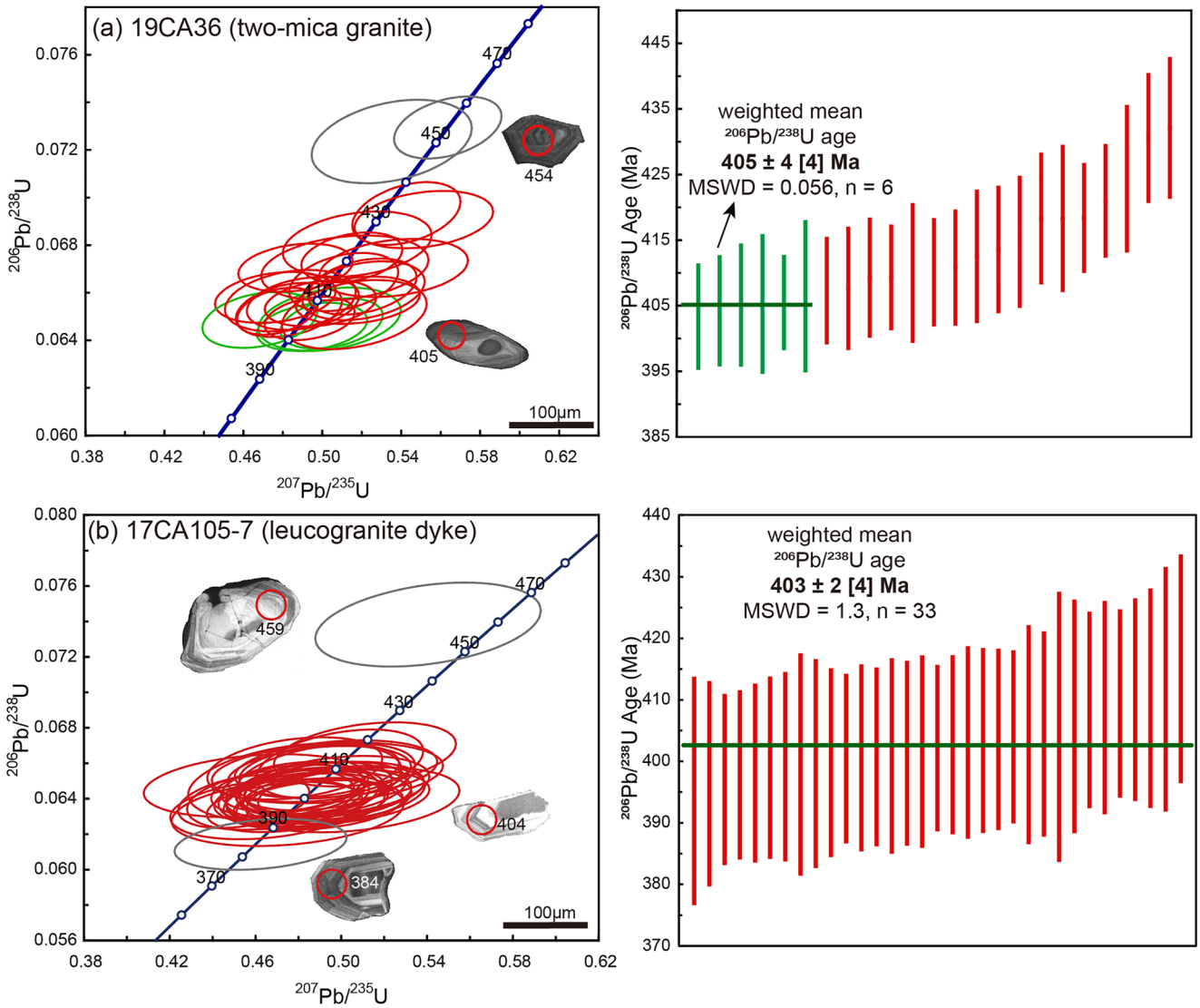

Figure 12. Zircon U-Pb concordia diagrams. Data excluded from the weighted mean age calculation are shown in gray circles. The data are presented in the format of A ± B [C] where A is the weighted mean age, B is the 2σ standard error of the mean, and C is the uncertainty of the measurement. See Figure 2 for location.

are reported at the 1σ level; mean ages for pooled U-Pb analyses are quoted at the 2σ level with a 95% confidence interval, and these original data are presented in Tables S1 and S2 in Supporting Information S1. For data reporting, an uncertainty of 1% (2RSD) that represents the long-term reproducibility of LA-ICP-MS monazite U-Pb geochronology is provided in addition to the 2σ standard error of the mean age (Horstwood et al., 2016). In such case, the data is presented in the format of A ± B [C]. A is the weighted mean age, B is the 2σ standard error of the mean, and C is the uncertainty (1%, 2RSD) of the measurement.

4.3. Results

4.3.1. Zircon U-Pb Age Dating

Zircon grains from the two-mica granite sample 19CA36 are mostly prisms, ~150–200 μm in length (aspect ratio 1:2–1:5), with subordinate subrounded grains. Nearly all grains exhibit igneous-related oscillatory zoning, except for a few grains that show dark luminescent cores in the CL images (Figure 12a). In both types of zircons, no metamorphic rims are observed. Twenty-five analyses were performed on the igneous-related portions, all of which have high Th/U ratios (>0.1). Twenty-three analyses yield concordant ages, ranging from 432 to 403 Ma.

19449194, 2022, 9, Downloaded from https://agupubs.onlinelibrary.wiley.com/doi/10.1029/2021TC007195 by Portail BibCNRS INSU, Wiley Online Library on [06/12/2023]. See the Terms and Conditions (https://onlinelibrary.wiley.com/terms-and-conditions) on Wiley Online Library for rules of use; OA articles are governed by the applicable Creative Commons License

19449194, 2022, 9, Downloaded from https://agupubs.onlinelibrary.wiley.com/doi/10.1029/2021TC007195 by Portail BibCNRS INSU, Wiley Online Library on [06/12/2023]. See the Terms and Conditions (https://onlinelibrary.wiley.com/terms-and-conditions) on Wiley Online Library for rules of use; OA articles are governed by the applicable Creative Commons License

Two other analyses yield slightly older ages around 450 Ma and these ages were interpreted as ages of inherited zircons. The six youngest ages form a tight cluster and give a weighted mean $^{206}Pb/^{238}U$ age of 405 ± 4 [4] Ma (MSWD = 0.056).

Zircon grains from sample 17CA105-7 have euhedral to sub-euhedral and prismatic shapes and are 80–150 μm in length with length/width ratios of 1:2–1:3. Most of the zircons display simple oscillatory zoning in their CL images, suggesting magmatic origins. Thirty-three analyses conducted on igneous-related portions define a simple and tight age population with a weighted mean $^{206}Pb/^{238}U$ age of 403 ± 2 [4] Ma (MSWD = 1.3) (Figure 12b). Besides, one analysis yields a relatively older age of ca. 459 Ma, interpreted as dating an inherited zircon.

4.3.2. Monazite U-Pb Age Dating

Monazite grains from samples 19CA41 and 19CA45-1 have similar morphological and internal structures. They are dominated by euhedral to subhedral, rounded to stubby grains, varying from 50 to 150 μm in length and 30–100 μm in width. In the BSE images, most grains display homogenous patchy structures (Figures 13a and 13b). Analyses of 23 grains of sample 19CA41 form a simple and tight age population with a weighted mean $^{206}Pb/^{238}U$ age of 412 ± 2 [4] Ma (MSWD = 1.3, Figure 13a). Twenty-five grains of sample 19CA45-1 were analyzed and yielded concordant and close ages, corresponding with a weighted mean $^{206}Pb/^{238}U$ age of 404 ± 1 [4] Ma (MSWD = 0.83, Figure 13b).

Monazite grains from sample 17CA107 are mostly anhedral with homogenous internal structures, 35 grains were analyzed and yielded concordant ages ranging from 463 to 391 Ma (Figure 13c). Among them, 34 analyses yielded ages ranging from 440 to 390 Ma with the majority of between 430 and 400 Ma with a prominent peak at ca. 412 Ma (Figure 13c). The remaining analysis is ~460 Ma (Figure 13c), which may represent the age of a xenocrystic grain.

Monazites in leucogranite sample 17CA105-4 are dominated by 80–150 μm stubby grains. Twenty-five spots on different grains were analyzed and the results yield concordant ages varying from 394 to 367 Ma with a prominent peak at ca. 379 Ma (Figure 13d).

Monazite grains from the pegmatite sample 19CA45-3 show subhedral shapes, ranging from 50 to 100 μm with length/width ratios between 1:1 and 1:2, and often contain mineral inclusions (Figure 13e). Twenty-five analyses were performed on different grains. Except for one less concordant analysis (the gray circle in the U-Pb concordia diagram), the remaining analyses yield concordant ages varying from 420 to 380 Ma with age peaks at ca. 406 and 382 Ma (Figure 13e).

5. Discussion

5.1. Structural and Metamorphic Evolution

The ubiquitous $S1_M$ foliation is represented by stromatic layering in the migmatitic Habahe Group rocks and schistosity in the greenschist- to amphibolite-facies Habahe Group rocks. This subhorizontal foliation is parallel to the original sedimentary bedding (S0) in the upper crustal rocks. In sites where $S1_M$ was folded by F2, subhorizontal fold hinges are always present (Figures 4d and 5e) which further confirms the originally subhorizontal attitude of $S1_M$. In migmatitic Habahe Group rocks, the subhorizontal $S1_M$ fabric is dominant planar structure that is associated with low-angle extensional lock-up shear bands filled with granitic leucosomes. These features suggest that the maximum principal shortening axis was vertical leading to horizontal extension during the $D1_M$ event (e.g., Cosgrove, 1997) as also suggested by Broussolle et al. (2018) and Jiang et al. (2019). Lack of mineral lineation on the $S1_M$ foliation was previously interpreted to reflect subvertical axial flattening associated with horizontal extension (Broussolle et al., 2018; Jiang et al., 2019) or it implies that high temperatures persisted after the extensional deformation erasing any preexisting lineation. Importantly, the horizontal migmatitic fabrics associated with recumbent rootless folds were reported in many places of the Chinese and Mongolian Altai (e.g., Hanžl et al., 2016; Jiang et al., 2019; Wang et al., 2021; Xu et al., 2021; Zhang et al., 2015) indicating the regional extent of this extensional regime.

In the migmatites, $S1_M$ foliation is associated with a garnet-sillimanite-K-feldspar-bearing assemblage (Figures 9a and 9b). Phase equilibrium modeling of similar mineral parageneses in neighboring areas suggested equilibration conditions roughly at 750–800°C/8 kbar, corresponding to anomalously hot metamorphic field gradients

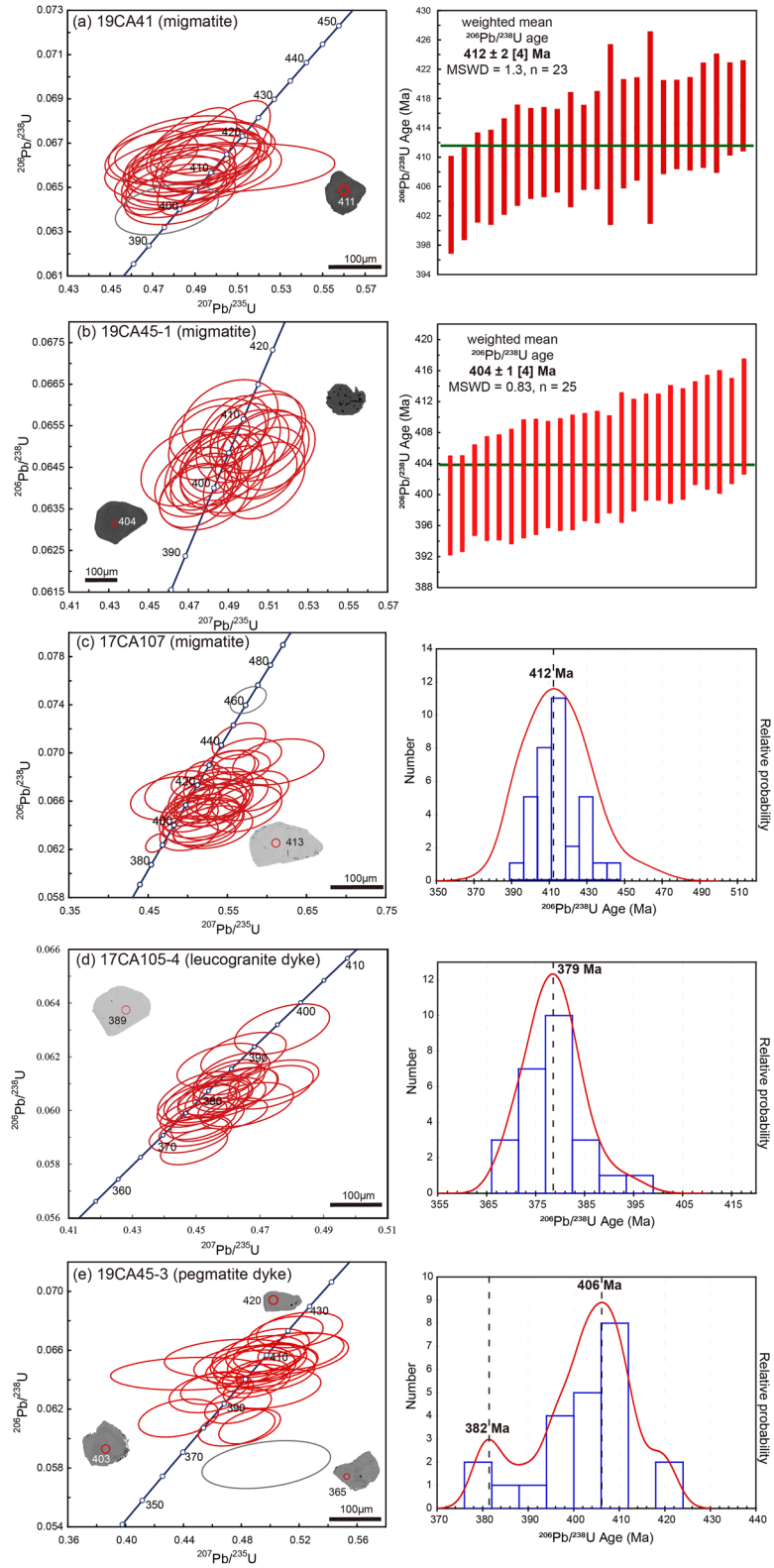

Figure 13. Monazite U-Pb concordia diagrams. Data excluded from the weighted mean age calculation are shown in gray circles. The data presented are in the same format as in Figure 12. See Figure 2 for sample location.

19449194, 2022, 9, Downloaded from https://agupubs.onlinelibrary.wiley.com/doi/10.1029/2021TC007195 by Portail BibCNRS INSU, Wiley Online Library on [06/12/2023]. See the Terms and Conditions (https://onlinelibrary.wiley.com/terms-and-conditions) on Wiley Online Library for rules of use; OA articles are governed by the applicable Creative Commons License

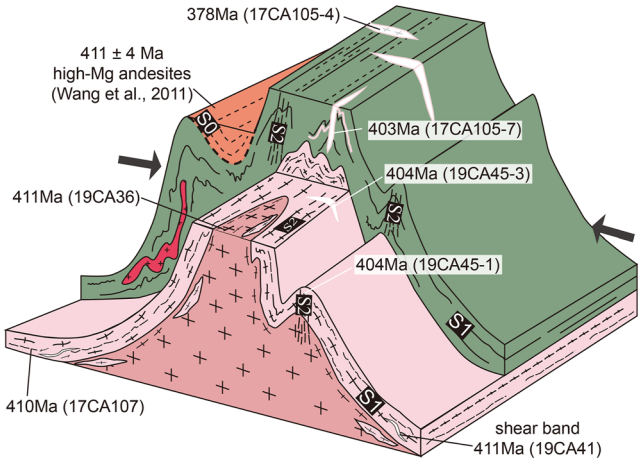

Figure 14. Interpretative sketch summarizing the structures and related geochronological data of the study area. Idealized locations of studied samples are indicated.

of 35°C/km or higher (Jiang et al., 2015, 2019; Wei et al., 2007), pointing to a high temperature and low-pressure (HT/LP) thermal regime. The $S1_M$ foliation in the low- to medium-grade domains of metamorphosed Habahe Group is associated with the syn-tectonic growth of cordierite suggesting the formation of this fabric also at HT/LP conditions. Similar HT/LP metamorphic gradient was also reported from the orogenic middle crust mica schist near the Aletai city (Jiang et al., 2022). There, re-equilibration of the staurolite stability field assemblage at an LP/HT stability field was proposed for sillimanite-bearing $S1_M$ fabric, with estimated thermal gradients shifting from ~23 to ~34°C/km (Jiang et al., 2022). These petrostructural observations are consistent with an extensional regime related to $D1_M$.

The tecono-thermal regime for the possible $D1_B$ is currently undetermined. However, relics of staurolite and/or kyanite preserved in compositionally zoned garnets have also been reported from migmatites across the Chinese Altai (Jiang et al., 2015, 2019). Chemistries of the garnets are compatible with a Barrovian-type prograde P-T evolution reaching a peak pressure at 8.7 kbar, corresponding to a crustal thickness of almost 30 km (Jiang et al., 2015, 2019; Wei et al., 2007). These findings suggest that $D1_B$ was possibly associated with moderate crustal thickening.

The $S1_M$ foliation was reworked by oblique and upright F2 folding associated with the development of the steep S2 fabric in high-strain zones or rotation of $S1_M$ into moderately dipping to subvertical attitudes in the low-strain domains. The resultant structures are predominantly N-S trending synforms occupied by Devonian metasedimentary rocks and antiforms cored by migmatites and granites (Figures 2 and 14). The N- or S-plunging F2 fold hinges and steeply dipping axial planes indicate a nearly E-W-directed subhorizontal shortening in current coordinates. Growth of cordierite and andalusite in the F2 planar leucosomes (Figures 9d–9h) suggests that the sillimanite-bearing $S1_M$ assemblage in the migmatitic Habahe Group rocks was re-equilibrated in low-pressure conditions. These features further indicate that the D2 folding was associated with the exhumation of migmatites to relatively shallower crustal levels. Such process has been described in other contractional orogens (e.g., Chopin et al., 2012; Soldner et al., 2020; Štípská et al., 2012) and is analogous to the large-scale doming associated with the extrusion of deep-seated orogenic lower crust described in other parts of the Chinese and Mongolian Altai (Broussolle et al., 2015; Jiang et al., 2015, 2019; Lehmann et al., 2017; Wang et al., 2021; Xu et al., 2021; Zhang et al., 2015).

The D3 effects are restricted to the southern part of the study area where originally N-S trending D2 fabrics were rotated into nearly E-W directions forming a map-scale F3 fold (Figure 2). In places, ~E-W trending greenschist-facies penetrative S3 foliation as well as D3 shear zones occur parallel with the southern limb of the F3 mega-fold (Figure 2).

The above petrostructural observations also allow quantifying the metamorphic P-T evolution of $D1_B$, $D1_M$, and D2. A simplified schematic P-T grid was produced using stabilities of index minerals retrieved from previous studies (Jiang et al., 2015; Wei et al., 2007). A prograde P-T path evolving along a typical Barrovian-type metamorphic field geothermal of 20°C/km is proposed in accordance with the presence of Barrovian-type mineral relics. The P-T path for the medium-grade domain would reach its peak in the staurolite-stability field and that for the migmatitic domain would be in the kyanite-stability field (e.g., Jiang et al., 2015). Previous metamorphic phase equilibria modeling suggested that peak conditions of $D1_B$-$M1_B$ in the medium-grade and migmatitic domains would have reached 560–590°C/6.0–7.0 kbar and 630°C/8.7 kbar, respectively (Figure 15, Jiang et al., 2015; Wei et al., 2007). Growth of cordierite in the $S1_M$ foliation of the medium-grade domains suggests a decompression P-T path from the staurolite-stability field to 4 kbar or lower. Yet, this evolution could be associated with the increase of temperature (Figure 15a). By contrast, the formation of garnet-sillimanite-K-feldspar-bearing assemblage associated with the $S1_M$ foliation of the migmatitic domain suggests a P-T evolution accompanied by a significant temperature increase and slight pressure decrease from kyanite to the sillimanite-K-feldspar stability fields. If the previous P-T estimates of 750–800°C/8 kbar from a similar S1 foliation in a neighboring migmatite (Jiang et al., 2015; Wei et al., 2007) is taken into account, a prograde P-T path roughly starting from ~630°C/8.7 kbar and ending at 750–800°C/8 kbar can be established for this migmatitic $S1_M$. It is apparent that the P-T evolution was

19449194, 2022, 9, Downloaded from https://agupubs.onlinelibrary.wiley.com/doi/10.1029/2021TC007195 by Portail BibCNRS INSU, Wiley Online Library on [06/12/2023]. See the Terms and Conditions (https://onlinelibrary.wiley.com/terms-and-conditions) on Wiley Online Library for rules of use; OA articles are governed by the applicable Creative Commons License

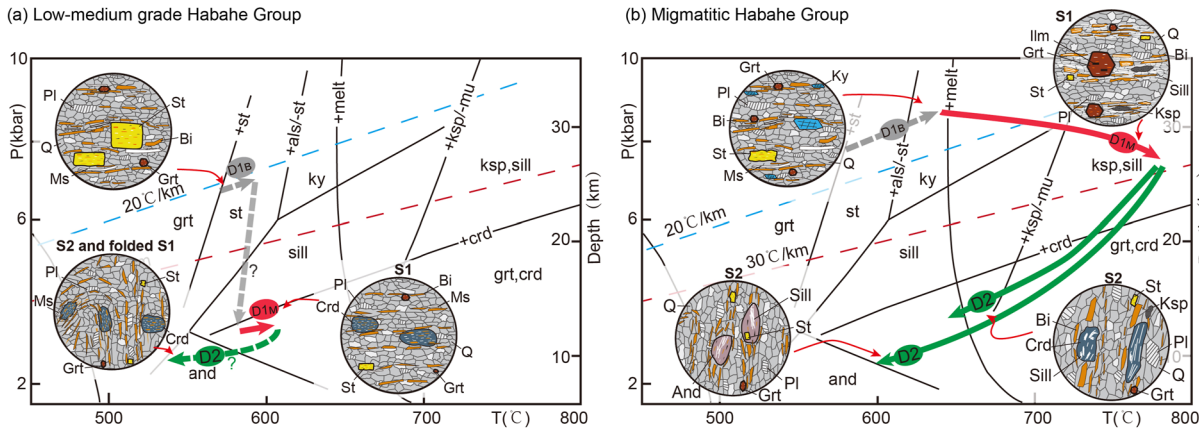

Figure 15. Qualitative P-T paths inferred for low-medium grade and migmatitic Habahe domains. Schematic mineral stability fields and two geotherms of 20 and 30°C/km, regarded as typical metamorphic gradients for the Barrovian and migmatite domains in the Altai, are from Wei et al. (2007) and Jiang et al. (2015). The wet granite solidus is after Ebadi and Johannes (1991).

associated with the switch of metamorphic gradients from medium-pressure/medium-temperature (~20°C/km) to low-pressure/high-temperature (>30°C/km) types (Figure 15b). It is therefore likely that both the medium-grade and migmatitic Habahe Group rocks shared heating and decompression evolution during $D1_M$.

The regional S2 foliation characterized by the growth of new cordierite and/or andalusite over the preexisting $D1_M$-$M1_M$ assemblage marks a retrograde P-T evolution. This would have started from 800°C/7 kbar ending at the solidus at the cordierite stability field. In the migmatites, this path can be taken down to the andalusite stability field at 4-3 kbar (Figure 15b). The D2-M2 petrostructural features of the medium-grade rocks, including replacement of the $S1_M$-cordierite by fine-grained muscovite and chlorite and crystallization of micas along S2, suggest a general D2-M2 retrograde evolution. Given that the medium-grade rocks are juxtaposed with higher grade migmatites, the former might have reached similar pressure conditions (and depths) as the latter during the retrograde evolution. A rough cooling P-T path can thus be proposed for the medium-grade rocks during D2 as shown in Figure 15a.

5.2. Geochronological Constraints on Individual Deformation Episodes

The study area has been the subject of many geochronological studies in recent years (Cai et al., 2011b; Sun et al., 2008, 2009; Wang et al., 2011). However, the age data have not been connected to structures, precluding estimation of timing and duration of individual deformational episodes.

Monazite grains from the $D1_M$ fabric can potentially retain the timing of the event. Migmatite samples 19CA41 and 17CA107 are characterized by subhorizontal $S1_M$ foliations associated with extensional shear bands. U-Pb monazite dating from these two samples covers a similar age range of 430-400 Ma with the clusters at ca. 412 ± 4 (1%, 2RSD). Such an age spread is also common in other samples. Given that monazites in migmatite are thought to form during cooling and crystallization of the melts (Morrissey et al., 2014), the age of ca. 412 Ma likely post-dates the main melting period and the $D1_M$ event could start as early as 430 Ma, since many monazites started to grow in that time (e.g., Figure 12a). This is supported by the dating of subhorizontal migmatitic foliations from the adjacent Tarlang migmatite-granite complex which yielded zircon U-Pb ages between 420 and 410 Ma (Wang et al., 2021). Accordingly, it can be concluded that the main melting process took place at least between 430 and 410 Ma. Such age spreads of the melting process are common in hot orogens worldwide, including the Lachlan orogenic belt in Australia (Collins, 2002a, 2002b; Foster & Gray, 2000; White & Chappell, 1988) and the Famatinian Orogen in Argentina (Farias et al., 2020; Wolfram et al., 2019). By contrast, the timing of $D1_B$ phase cannot be precisely determined by the current geochronological data. However, the relative timing of the $D1_B$ can be bracketed by the Late Ordovician deposition of the protolith of the metamorphic sequence and onset $D1_M$ event which is dated at least prior to 430 Ma as discussed above. This is also supported by the fact that $S1_B$ foliation is crosscutting by ca. 400 Ma granites reported near the Aletai city to the east (Jiang et al., 2019). In addition, Barrovian metamorphism ($D1_B$) in the Hovd region of the Altai wedge to the north was determined at

19449194, 2022, 9, Downloaded from https://agupubs.onlinelibrary.wiley.com/doi/10.1029/2021TC007195 by Portail BibCNRS INSU, Wiley Online Library on [06/12/2023]. See the Terms and Conditions (https://onlinelibrary.wiley.com/terms-and-conditions) on Wiley Online Library for rules of use; OA articles are governed by the applicable Creative Commons License

ca. 455 Ma by Soejono et al. (2021), advocating the latest Ordovician to Early Silurian Barrovian metamorphism across the Altai wedge.

The remaining zircon and monazite U-Pb ages constrain the timing of D2 event. Sample 19CA45-1 with monazite U-Pb age of 404 ± 1 [4] Ma was collected from the migmatitic Habahe Group domain and shows nearly complete transposition of S1 foliation by S2 fabric (Figure 13c). Samples 19CA36 and 19CA105-7 from syn-D2 granite intrusions yielded zircon U-Pb crystallization ages of 405 ± 4 [4] and 403 ± 2 [4] Ma, respectively (Figure 12), which is identical within the analytical uncertainties to the monazite U-Pb age of sample 19CA45-1. These ages are slightly younger than those of the discussed above migmatitic samples with well-preserved $S1_M$ foliation and such a small age discrepancy probably reflects the transition from D1 horizontal to D2 vertical flows, probably indicating a gradual change from D1 to D2. This is in agreement with structural observations suggesting that syn-D1 melt was still present at the onset of D2. Finally, leucogranite dyke sample 17CA105-4 and pegmatite dyke sample 19CA45-3, emplaced along the syn-D2 tensional fractures, gave ages varying between 420 and 370 Ma (Figures 13d and 13e) with age peaks at 379 and 382 Ma, suggesting that the final crystallization of the dykes occurred late or after D2. These ages may suggest propagation of tensional fractures and dyke emplacement due to progressive locking of F2 folds connected to cooling and embrittlement of the whole edifice during the Middle Devonian.

Compared with D1 and D2, the timing of the D3 in the study area is currently undetermined. Nevertheless, Zhang et al. (2015) and Wang et al. (2018) conducted detailed geochronological analyses in the southern limb of the F3 mega-fold and proposed that the D3 event occurred at 275-267 Ma.

5.3. Tectonic Evolution and Geodynamic Implications

Data presented above alongside recent data from Jiang et al. (2019), Wang et al. (2021), and Jiang et al. (2022) provide a basis for chronological correlations across the Chinese Altai. In particular, when available data from the Chinese Altai are integrated with those from the Hovd Zone to the north (Soejono et al., 2021), the East Junggar domain to the south (Li et al., 2019, 2020; Long et al., 2012; Zhang et al., 2008), and the Gobi-Altai Zone from the southern Mongolian Altai to the east (Broussolle et al., 2015; Lehmann et al., 2017), the temporal and spatial characteristics of the suprasubduction evolution of the whole Altai accretionary system is addressed below.

5.3.1. Suprasubduction Deformation of the Accretionary Wedge

The Altai represented an immense Early Paleozoic accretionary wedge developed at the periphery of the ~1,800 km long active continental margin of the Tuva-Mongolian continental ribbons (Jiang et al., 2017; Xiao et al., 2009). The wedge was formed due to a prominent retreat of the Panthalassa subduction system, which also formed the ca. 520-460 Ma, an ~1,800-km-long Ikh-Mongol Arc System (Figure 16a, Janoušek et al., 2018; Jiang et al., 2017). Subsequently, the Altai wedge was affected by an important Barrovian metamorphic event (Jiang et al., 2015; Wei et al., 2007) associated with tectonic burial and moderate thickening (Jiang et al., 2015, 2019; Wei et al., 2007), which has recently been dated at ca. 455 Ma in the Hovd Zone and Mongolian Altai (Burenjargal et al., 2014; Soejono et al., 2021). These features suggest that the Altai was shortened during the Late Ordovician to Early Silurian indicating that the Cambro-Ordovician subduction zone retreat switched to an advancing mode during this period (Figure 15b).

During the Late Silurian to Middle Devonian, the Altai crust was significantly stretched and thinned, in particular, in its Chinese sector. This is exemplified by (a) extensional structures associated with decompressional P-T evolution in the orogenic lower crust migmatitic domains (Figure 15b, Jiang et al., 2015), (b) decompressional P-T evolution in the orogenic middle crust medium-grade Habahe Group (Figure 15a, Jiang et al., 2022), and (c) formation of upper crust Devonian extensional basins filled by volcanic rocks with bimodal geochemical characteristics (Cui et al., 2020; Wan et al., 2011). Coeval with the generalized extensional regime in the Chinese Altai, within-plate and alkaline magmatism was also documented in the NE part of the Altai wedge, that is, Hovd Zone to the north, which was interpreted as reflecting a localized extension (Soejono et al., 2017). Contemporaneously, an arc system developed further south in the East Junggar domain as well as the neighboring Trans-Altai region (Kröner et al., 2010; Li et al., 2019; Nguyen et al., 2018; Xiao et al., 2009; Zhang et al., 2008). Recent studies have suggested that the Altai wedge and the East Junggar were separated by a small oceanic basin that closed in the Early Permian (Jiang et al., 2019; Laurent-Charvet et al., 2003; Li et al., 2017; Qu & Zhang, 1994). The Middle Devonian Kuerti ophiolitic fragments with back-arc basin geochemical affinities, are located in between

19449194, 2022, 9, Downloaded from https://agupubs.onlinelibrary.wiley.com/doi/10.1029/2021TC007195 by Portail BibCNRS INSU, Wiley Online Library on [06/12/2023]. See the Terms and Conditions (https://onlinelibrary.wiley.com/terms-and-conditions) on Wiley Online Library for rules of use; OA articles are governed by the applicable Creative Commons License

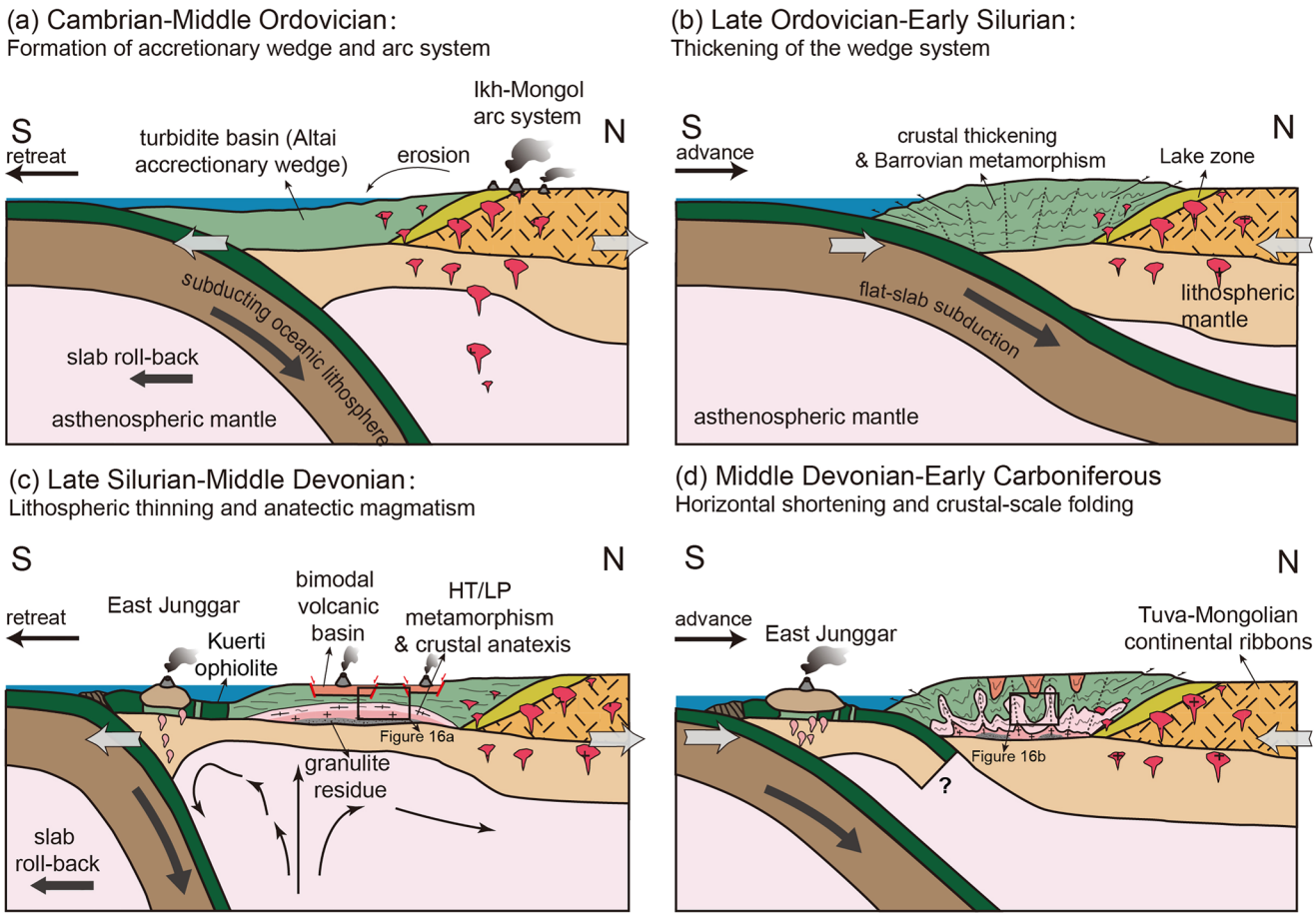

Figure 16. Tectonic sketches correlating Cambrian to Carboniferous tectono-thermal evolution of the Altai accretionary wedge with alternating advancing and retreating of subduction. (a) Cambrian-Middle Ordovician subduction retreat gave rise to the formation of the Ikh-Mongol Arc and a turbidite basin (future Altai wedge); (b) Late Ordovician-Early Silurian subduction advance caused thickening and Barrovian metamorphism in the Altai wedge sequence; (c) Late Silurian-Middle Devonian subduction retreat was responsible for crustal extension in the Altai and migration of arc fronts into the East Junggar; and (d) Middle Devonian-Early Carboniferous subduction advance generated crustal-scale D2 folding.

the Chinese Altai and the East Junggar domain (Xu et al., 2003). These were interpreted as marking the site of the oceanic basin cited above (Long et al., 2012). Available detrital zircon age data collected from the pre-Permian sedimentary sequences of both East Junggar-Trans-Altai Zone and the Altai accretionary wedge (Table S3 in Supporting Information S1) show that the former preserve a large number of pre-Silurian detrital zircons (Figure S1 in Supporting Information S1) and have detrital age patterns not comparable with any known local magmatic rocks but resemble to those commonly reported in the Altai wedge (Figure S1 in Supporting Information S1, Long et al., 2012). These features led many authors to suggest that the East Junggar domain was a stretched margin of the Altai wedge and developed a typical Devono-Carboniferous marginal sea-island arc system (Li et al., 2019; Long et al., 2012). Spreading of the back-arc basin was most likely responsible for the stretching of the Altai crust when the East Junggar drifted away from the Altai wedge. The spatial and temporal relations among the Altai wedge in the north, the back-arc basin in the middle, and the East Junggar arc system in the south are consistent with northward subduction (Figure 16). Taken together, extensional tectonics in the Chinese Altai and migration of arc fronts south to the East Junggar probably reflect a retreat of the subduction system during the Devonian (Figure 16c).

This extensional event was followed by the Middle-Late Devonian upright D2 folding. Partially molten crust inherited from the $D1_M$ extension probably strongly weakened the lower crust during this compressional deformation (Jamieson & Beaumont, 2011; Maierová et al., 2016). The presence of melt in the crust at this time is indicated by the migration of anatectic magma to shallower crustal levels as indicated by F2 axial planar leucosomes associated with the growth of andalusite- and/or cordierite-bearing low-pressure assemblages (Figure 15b).

19449194, 2022, 9, Downloaded from https://agupubs.onlinelibrary.wiley.com/doi/10.1029/2021TC007195 by Portail BibCNRS INSU, Wiley Online Library on [06/12/2023]. See the Terms and Conditions (https://onlinelibrary.wiley.com/terms-and-conditions) on Wiley Online Library for rules of use; OA articles are governed by the applicable Creative Commons License

19449194, 2022, 9, Downloaded from https://agupubs.onlinelibrary.wiley.com/doi/10.1029/2021TC007195 by Portail BibCNRS INSU, Wiley Online Library on [06/12/2023]. See the Terms and Conditions (https://onlinelibrary.wiley.com/terms-and-conditions) on Wiley Online Library for rules of use; OA articles are governed by the applicable Creative Commons License

Contemporaneous injection of anatectic crust in cores of regional F2 antiforms has also been already reported in the Chinese Altai (Jiang et al., 2015, 2019; Wang et al., 2021; Zhang et al., 2015) as well as in the neighboring Mongolian Altai (Broussolle et al., 2015; Lehmann et al., 2017). We argue that such a tectonic style can be best explained by the shortening of heterogeneously extended, partially molten, and stratified crust.

The regional shortening regime also affected the East Junggar arc system to the south. This is recorded by sedimentary rocks that suggest a switch of depositional environment from a marine transgressional sequence (the Beitashan Formation) during the Middle Devonian to a marine regressional sequence (the Yundukala and Kaxiweng Formation) during the Middle-Late Devonian (Wu, 2018), implying progressive closure of oceanic basins. In addition, in the East Junggar angular unconformities have also been observed between the Middle Devonian volcano-clastic sequence and its overlying Early Carboniferous clastic sequence (e.g., the Nanmingshui Formation) (Li et al., 2020). Another unconformity has also been reported between the Late Devonian and Early Carboniferous sedimentary basins from the neighboring Gobi-Altai Zone of southern Mongolian Altai. This has been interpreted as marking the development of intramontane basins in response to an important crustal shortening (Kröner et al., 2010; Lehmann et al., 2010; Markova, 1975).

Taken together, the Altai and its southerly Junggar arc system were jointly affected by a prominent Middle Devonian to Early Carboniferous crustal shortening, soon after the crustal extension $D1_M$ event. Such a switch of tectonic style may reflect a succession of retreating and advancing subduction mode (Figure 16d).

5.3.2. Devonian Anomalous Heat Input and Heterogeneous Stretching of the Altai Crust in Response to Subduction Zone Retreat

Crustal extension associated with subduction retreat would in theory cause significant thermal perturbation of the overriding plate (Jolivet et al., 1998). In the Altai, the extension is accompanied by anatexis in the lower orogenic crust (Broussolle et al., 2015; Jiang et al., 2015, 2019; Zhang et al., 2015). In addition, the overlying Devonian sequences contain high-Mg andesites and bimodal volcanic rocks (Cui et al., 2020; Soejono et al., 2018; Wan et al., 2010; Wang et al., 2011) coeval with the intrusion of Circum-Pacific S-type granitoids (Huang et al., 2020; Jiang et al., 2016), emplacement of mafic rocks (Niu et al., 2006; Wong et al., 2010), and development of VMS mineralization (Wan et al., 2010, 2011). All these phenomena are the hallmark of a significant increase of the heat budget of the entire Altai crust during the Devonian. The anomalous thermal regime is further supported by isotopic signatures that show abrupt changes in Devonian times. For example, Hf isotopic compositions of igneous zircons show a marked change at 420 Ma from $\varepsilon_{Hf}(t) = -18 - +15$ at >420 Ma, to $\varepsilon_{Hf}(t) = 0 - +16$ at <420 Ma (Sun et al., 2009). Likewise, the $\delta^{18}O$ values (ranging from 0.89 to 16.29‰) are negatively correlated with Hf isotope values and also show a sharp decreasing trend at ca. 420-380 Ma (Zhang et al., 2020). These features indicate the contribution of a juvenile mantle in magma source associated with uncommonly elevated heat flux, possibly due to the upwelling of the hot asthenosphere beneath the Altai accretionary wedge resulting from extension associated with the subduction zone retreat.

Another prominent geological feature of the Altai crust in response to this retreat is the heterogeneous crustal thinning and the crustal anatexis. For instance, the orogenic middle crustal Habahe Group rocks recorded crustal thinning of ~8–10 km reflected by the pressure drop of ~2–3 kbar from MP/MT Barrovian peak conditions to LP/HT cordierite-bearing assemblage (Figures 17a–17c). Likewise, a slightly smaller pressure drop of ~1 kbar was recorded by the orogenic lower crustal migmatites (Figures 17a–17c). This smaller discrepancy in pressure drop with respect to the orogenic middle crust suggests heterogeneous thinning of the orogenic suprastructure and infrastructure. Notably, the orogenic lower crustal migmatite-granite complex in the neighboring southerly Taerlang area is in direct contact with the upper crustal Devonian volcano-clastic rocks (Jiang et al., 2015; Wang et al., 2021). In addition to the thinning of F2 limbs during postbuckle D2 flattening (Jiang et al., 2019), extreme thinning of the orogenic middle crust along a possible localized detachment zone was most likely another main mechanism accounting for such contact. Such heterogeneous crust stretching is common in extensional metamorphic core complexes worldwide (Figure 17a, Jolivet et al., 2021; Lister & Baldwin, 1993; Tirel et al., 2008; Wickham & Oxburgh, 1986). It is likely that the Chinese Altai was also probably affected by the growth of extensional core complexes associated with heterogeneous thinning of the orogenic crust during the Devonian subduction retreat, even no solid evidence for this has yet been recognized in the region.

Later, the molten orogenic lower crust was vertically extruded in the cores of regional F2 antiforms, probably assisted by the interplay between D2 horizontal shortening and magma diapirism (Wang et al., 2021).

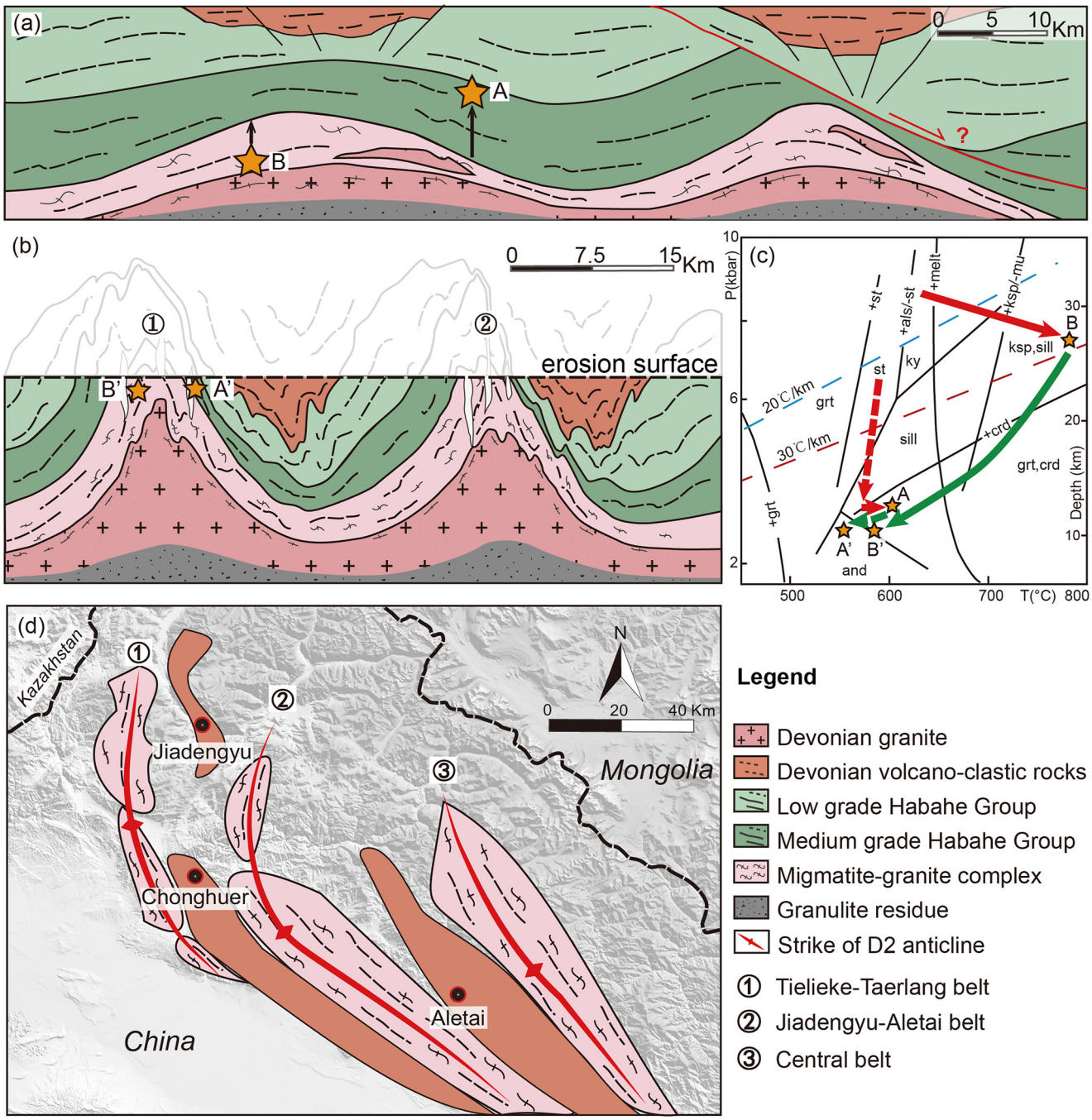

Figure 17. (a) Heterogeneous deformation of the crust and growth of extensional core complexes with respect to subduction retreating. Idealized locations of samples from medium-grade Habahe Group (approximately orogenic middle crust) and migmatitic Habahe Group (approximately orogenic lower crust) are indicated; (b) Formation of migmatite-granite domal structures during crustal shortening (vertical axes not to scale); (c) Inferred P-T data shows that discrepancy in pressure drops between the orogenic middle and lower crust, indicating heterogeneous deformation characteristics of the Altai crust during alternating extension and shortening cycle. See the text for detailed explanations; and (d) Spatial distribution of the migmatite-granite complex and Devonian volcanic basins across the Chinese Altai showing alternating core and basin structures.

Consequently, the preexisting crustal architecture was further exploited during D2 shortening which resulted in further amplification of core complexes and formation of narrow migmatite-granite domal structures alternating with shortened Devonian basins (e.g., Wang et al., 2021, Figures 16c, 16d, 17a, and 17d).

19449194, 2022, 9, Downloaded from https://agupubs.onlinelibrary.wiley.com/doi/10.1029/2021TC007195 by Portail BibCNRS INSU, Wiley Online Library on [06/12/2023]. See the Terms and Conditions (https://onlinelibrary.wiley.com/terms-and-conditions) on Wiley Online Library for rules of use; OA articles are governed by the applicable Creative Commons License

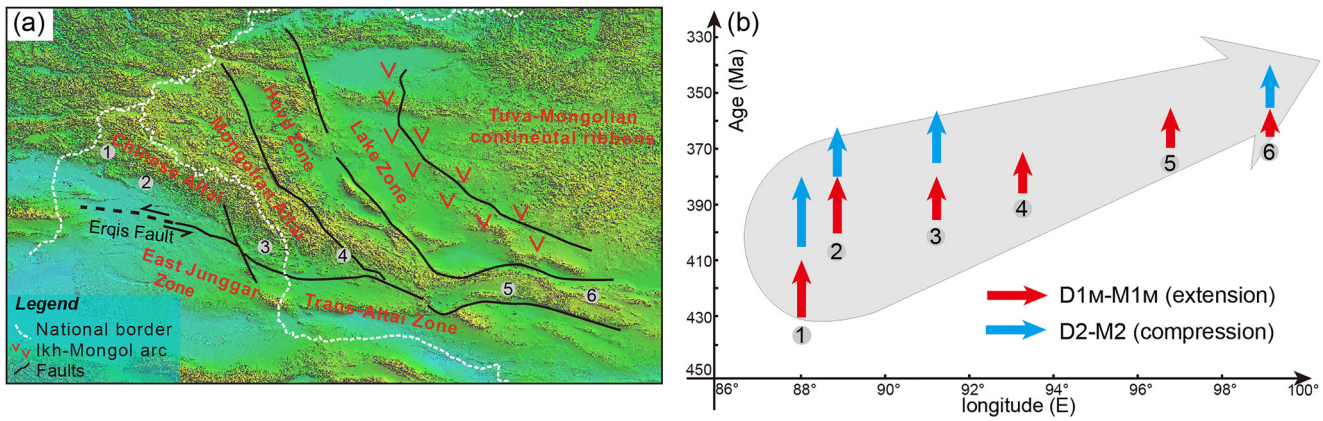

Figure 18. (a) Topographic map of the Mongolian Collage System with main tectono-lithological units indicated (modified after Li et al., 2019). Six representative localities along-strike of the Altai Range which recorded the Devonian extension-compressional cycle are shown: (1) the study area, (2) Aletai, (3) Qinghe, (4) the western Tseel unit, (5) the eastern Tseel unit, and (6) the Chandman massif; (b) Timing of the Devonian $D1_M$ extension and -D2 compression deformation in the areas in (a) versus longitude showing eastward migration of the extension-compression cycle. Data sources: (1) $D1_M$: 430-410 Ma, D2: 405-379 Ma (this study), (2) $D1_M$: 400-380 Ma, D2: 380 Ma (Jiang et al., 2019), (3) $D1_M$: 394 Ma, D2: 380-370 Ma (Xu et al., 2021), (4) $D1_M$: 385 Ma (Jiang et al., 2012), (5) $D1_M$: 370 Ma (Burenjargal et al., 2014; Hanžl et al., 2016), and (6) $D1_M$: 367-356 Ma, D2: 356-340 Ma (Broussolle et al., 2015).

5.3.3. Regional Migration of Extension-Shortening Cycle Across the Altai Wedge

The extension event between 420 and 405 Ma followed by regional shortening between 400 and 370 Ma roughly corresponds to those of Soejono et al. (2021) from the northerly Hovd Zone in Mongolia where crustal extension between 435 and 400 Ma was followed by intensive shortening between 385 and 350 Ma. However, the geochronological and structural data in southern Mongolian Altai, 400 km east of the studied region, suggest that the crustal extension started at 400 Ma culminating after 380 Ma (Hanžl et al., 2016) and syn-compressional growth of the migmatite domes started at 360 Ma and culminated at around 340 Ma (Broussolle et al., 2015; Lehmann et al., 2017). When combining the extension-compression timing data from the Aletai city (Jiang et al., 2019), Qinghe (Xu et al., 2021), and different parts of the Tseel unit and Chandman massif in southern Mongolian Altai (Broussolle et al., 2015; Burenjargal et al., 2014; Jiang et al., 2012), it is apparent that there is a younging trend of cycle from west to the east (Figure 18), occurring ca 30–40 Ma later in the southern Mongolian Altai compared to the Chinese Altai. Such temporal and spatial shifts along the convergent margin were probably related to variations in the rates of slab rollback, perhaps due to the subduction of inhomogeneous oceanic lithosphere, similar to processes documented in the southwest Pacific (Schellart et al., 2002; Shaanan et al., 2014). Further tuning of this model in the Altai region is needed, calling for the extension of similar types of studies to the west in Russia and to the east in Mongolia.

6. Conclusions

Petrostructural and petro-chronological analyses presented constrain the geometries, kinematics, and timing of the Devonian fabrics in the NW Chinese Altai. When combined with regional data, the Devonian tectonic evolution across the Altai accretionary system lead to the following conclusions:

1. A subhorizontal high-temperature/low-pressure S1 fabric associated with crustal anatexis developed during stretching and thinning of the crust related to Early-Middle Devonian extension.
2. The stretched and thermally softened crust then underwent ~E-W shortening during the Mid- Devonian D2 event that formed steep ~N-S trending D2 antiforms and synforms which led to juxtapositions of contrasting crustal levels.
3. The structural evolution of the Chinese Altai can be interpreted as a result of an extension-compression cycle reflecting variations in subduction dynamics between slab advance and retreat. A multiple phase of alternating subduction zone advance and retreat governed the formation and subsequent geological reworking of the entire Altai accretionary wedge from the Ordovician to the Carboniferous. This tectonic switch from extension to shortening shows a 30–40 Ma younging eastward along strike of the accretionary front indicative of lateral inhomogeneities in the nature of the subduction oceanic lithosphere.

19449194, 2022, 9, Downloaded from https://agupubs.onlinelibrary.wiley.com/doi/10.1029/2021TC007195 by Portail BibCNRS INSU, Wiley Online Library on [06/12/2023]. See the Terms and Conditions (https://onlinelibrary.wiley.com/terms-and-conditions) on Wiley Online Library for rules of use; OA articles are governed by the applicable Creative Commons License

Data Availability Statement

The geochronological data of this study are included in the Supporting Information. Data used in this study are currently being archived in the Pangaea data repository: https://doi.org/10.1594/PANGAEA.942545.

Acknowledgments
This project was supported by the National Natural Science Foundation of China (grant nos. 42022017, 42021002, and 42025204) and the International Partnership Program of Chinese Academy of Sciences (No. 132744KYSB20190039). The Czech Science Foundation (GACR grant no. EXPRO 19-27682X) to K.Schulmann is also acknowledged. Pengfei Li is acknowledged for discussion. We wish to also thank Kang Xu and Ming Xiao for their help during our field investigation. Constructive reviews from W.J. Xiao and W. J. Collins and editorial suggestions from Federico Rossetti resulted in significant improvements to the paper.

References

Aleinikoff, J. N., Schenck, W. S., Plank, M. O., Srogi, L. A., Fanning, C. M., Kamo, S. L., & Bosbyshell, H. (2006). Deciphering igneous and metamorphic events in high-grade rocks of the Wilmington Complex, Delaware: Morphology, cathodoluminescence and backscattered electron zoning, and SHRIMP U-Pb geochronology of zircon and monazite. *The Geological Society of America Bulletin*, *118*(1–2), 39–64. https://doi.org/10.1130/b25659.1

Broussolle, A., Aguilar, C., Sun, M., Schulmann, K., Štípská, P., Jiang, Y., et al. (2018). Polycyclic Palaeozoic evolution of accretionary orogenic wedge in the southern Chinese Altai: Evidence from structural relationships and U-Pb geochronology. *Lithos*, *314*, 400–424. https://doi.org/10.1016/j.lithos.2018.06.005

Broussolle, A., Štípská, P., Lehmann, J., Schulmann, K., Hacker, B. R., Holder, R., et al. (2015). P-T-t-D record of crustal-scale horizontal flow and magma-assisted doming in the SW Mongolian Altai. *Journal of Metamorphic Geology*, *33*(4), 359–383. https://doi.org/10.1111/jmg.12124

Broussolle, A., Sun, M., Schulmann, K., Guy, A., Aguilar, C., Štípská, P., et al. (2019). Are the Chinese Altai "terranes" the result of juxtaposition of different crustal levels during Late Devonian and Permian orogenesis? *Gondwana Research*, *66*, 183–206. https://doi.org/10.1016/j.gr.2018.11.003

Burenjargal, U., Okamoto, A., Kuwatani, T., Sakata, S., Hirata, T., & Tsuchiya, N. (2014). Thermal evolution of the Tseel terrane, SW Mongolia and its relation to granitoid intrusions in the Central Asian Orogenic Belt. *Journal of Metamorphic Geology*, *32*(7), 765–790. https://doi.org/10.1111/jmg.12090

Cai, K. D., Sun, M., Yuan, C., Long, X. P., & Xiao, W. J. (2011). Geological framework and paleozoic tectonic history of the Chinese Altai, NW China: A review. *Russian Geology and Geophysics*, *52*(12), 1619–1633. https://doi.org/10.1016/j.rgg.2011.11.014

Cai, K. D., Sun, M., Yuan, C., Zhao, G. C., Xiao, W. J., Long, X. P., & Wu, F. Y. (2011a). Geochronology, petrogenesis and tectonic significance of peraluminous granites from the Chinese Altai, NW China. *Lithos*, *127*(1–2), 261–281. https://doi.org/10.1016/j.lithos.2011.09.001

Cai, K. D., Sun, M., Yuan, C., Zhao, G. C., Xiao, W. J., Long, X. P., & Wu, F. Y. (2011b). Prolonged magmatism, juvenile nature and tectonic evolution of the Chinese Altai, NW China: Evidence from zircon U-Pb and Hf isotopic study of Paleozoic granitoids. *Journal of Asian Earth Sciences*, *42*(5), 949–968. https://doi.org/10.1016/j.jseaes.2010.11.020

Cawood, P. A., Kröner, A., Collins, W. J., Kusky, T. M., Mooney, W. D., & Windley, B. F. (2009). Accretionary orogens through Earth history. *Earth Accretionary Systems in Space and Time*, *318*(1), 1–36. https://doi.org/10.1144/sp318.1

Chopin, F., Schulmann, K., Skrzypek, E., Lehmann, J., Dujardin, J., Martelat, J., et al. (2012). Crustal influx, indentation, ductile thinning and gravity redistribution in a continental wedge: Building a Moldanubian mantled gneiss dome with underthrust Saxothuringian material (European Variscan belt). *Tectonics*, *31*(1). https://doi.org/10.1029/2011TC002951

Collins, W. J. (2002a). Hot orogens, tectonic switching, and creation of continental crust. *Geology*, *30*(6), 535–538. https://doi.org/10.1130/0091-7613(2002)030<0535:Hotsac>2.0.Co;2

Collins, W. J. (2002b). Nature of extensional accretionary orogens. *Tectonics*, *21*(4), 6-1–6-12. https://doi.org/10.1029/2000tc001272

Collins, W. J., & Richards, S. W. (2008). Geodynamic significance of S-type granites in circum-Pacific orogens. *Geology*, *36*(7), 559–562. https://doi.org/10.1130/G24658a.1

Cosgrove, J. W. (1997). The influence of mechanical anisotropy on the behaviour of the lower crust. *Tectonophysics*, *280*(1–2), 1–14. https://doi.org/10.1016/S0040-1951(97)00145-5

Cui, X., Sun, M., Zhao, G. C., Yao, J. L., Zhang, Y. Y., Han, Y. G., & Dai, L. M. (2020). A Devonian arc-back-arc basin system in the southern Chinese Altai: Constraints from geochemical and Sr-Nd-Pb isotopic data for meta-basaltic rocks. *Lithos*, *366*, 105540. https://doi.org/10.1016/j.lithos.2020.105540

Donskaya, T. V., Sklyarov, E. V., Gladkochub, D. P., Mazukabzov, A. M., Sal'nikova, E. B., Kovach, V. P., et al. (2000). The Baikal collisional metamorphic belt. *Doklady Earth Sciences*, *374*(7), 1075–1079.

Ebadi, A., & Johannes, W. (1991). Beginning of melting and composition of first melts in the system Qz-Ab-Or-H_2O-CO_2. *Contributions to Mineralogy and Petrology*, *106*(3), 286–295. https://doi.org/10.1007/bf00324558

Eizenhofer, P. R., Zhao, G. C., Zhang, J., & Sun, M. (2014). Final closure of the Paleo-Asian Ocean along the Solonker suture zone: Constraints from geochronological and geochemical data of Permian volcanic and sedimentary rocks. *Tectonics*, *33*(4), 441–463. https://doi.org/10.1002/2013tc003357

Farias, P., Weinberg, R., Sola, A., & Becchio, R. (2020). From crustal thickening to orogen-parallel escape: The 120-Myr-long HT-LP evolution recorded by Titanite in the Paleozoic Famatinian Backarc, NW Argentina. *Tectonics*, *39*(9), e2020TC006184. https://doi.org/10.1029/2020tc006184

Fossen, H. (2010). *Structural geology*. Cambridge University Press.

Foster, D. A., & Gray, D. R. (2000). Evolution and structure of the Lachlan fold belt (orogen) of eastern Australia. *Annual Review of Earth and Planetary Sciences*, *28*(1), 47–80. https://doi.org/10.1146/annurev.earth.28.1.47

Foster, D. A., Gray, D. R., Spaggiari, C., Kamenov, G., & Bierlein, F. P. (2009). Palaeozoic Lachlan orogen, Australia; accretion and construction of continental crust in a marginal ocean setting: Isotopic evidence from Cambrian metavolcanic rocks. *Earth Accretionary Systems in Space and Time*, *318*(1), 329–349. https://doi.org/10.1144/sp318.12

Gladkochub, D. P., Donskaya, T. V., Wingate, M. T. D., Poller, U., Kröner, A., Fedorovsky, V. S., et al. (2008). Petrology, geochronology, and tectonic implications of c. 500 Ma metamorphic and igneous rocks along the northern margin of the Central Asian Orogen (Olkhon terrane, Lake Baikal, Siberia). *Journal of the Geological Society*, *165*(1), 235–246. https://doi.org/10.1144/0016-76492006-125

Glen, R. A. (2013). Refining accretionary orogen models for the Tasmanides of eastern Australia. *Australian Journal of Earth Sciences*, *60*(3), 315–370. https://doi.org/10.1080/08120099.2013.772537

Guy, A., Schulmann, K., Soejono, I., Holzrichter, N., Lexa, O., & Munschy, M. (2021). Structures and geodynamics of the Mongolian tract of the Central Asian Orogenic Belt constrained by potential field analyses. *Gondwana Research*, *92*, 26–53. https://doi.org/10.1016/j.gr.2020.11.016

Guy, A., Schulmann, K., Soejono, I., & Xiao, W. (2020). Revision of the Chinese Altai-East Junggar terrane accretion model based on Geophysical and geological constraints. *Tectonics*, *39*(4), e2019TC006026. https://doi.org/10.1029/2019tc006026

19449194, 2022, 9, Downloaded from https://agupubs.onlinelibrary.wiley.com/doi/10.1029/2021TC007195 by Portail BibCNRS INSU, Wiley Online Library on [06/12/2023]. See the Terms and Conditions (https://onlinelibrary.wiley.com/terms-and-conditions) on Wiley Online Library for rules of use; OA articles are governed by the applicable Creative Commons License

Han, Q., Zhao, T., Tang, Z., Zheng, J., Wang, T., Li, C., et al. (2016). Zircon U-Pb age and its geological significance of Biliewutixi rock Body in Western Altay mountains. *Xinjiang Geology*, *34*(1), 46–53. (in Chinese with English abstract).

Hanžl, P., Schulmann, K., Janoušek, V., Lexa, O., Hrdličková, K., Jiang, Y., et al. (2016). Making continental crust: Origin of Devonian orthogneisses from SE Mongolian Altai. *Journal of Geosciences*, *61*(1), 25–50. https://doi.org/10.3190/jgeosci.206

Horstwood, M. S. A., Košler, J., Gehrels, G., Jackson, S. E., McLean, N. M., Paton, C., et al. (2016). Community-derived standards for LA-ICP-MS U-(Th-)Pb geochronology–uncertainty propagation, age interpretation and data reporting. *Geostandards and Geoanalytical Research*, *40*(3), 311–332. https://doi.org/10.1111/j.1751-908X.2016.00379.x

Huang, Y. Q., Jiang, Y. D., Collett, S., Wang, S., Xu, K., Shu, T., et al. (2020). Magmatic recycling of accretionary wedge: A new perspective on Silurian-Devonian I-type granitoids generation in the Chinese Altai. *Gondwana Research*, *78*, 291–307. https://doi.org/10.1016/j.gr.2019.07.019

Jamieson, R. A., & Beaumont, C. (2011). Coeval thrusting and extension during lower crustal ductile flow-implications for exhumation of high-grade metamorphic rocks. *Journal of Metamorphic Geology*, *29*(1), 33–51. https://doi.org/10.1111/j.1525-1314.2010.00908.x

Janoušek, V., Jiang, Y., Buriánek, D., Schulmann, K., Hanžl, P., Soejono, I., et al. (2018). Cambrian-Ordovician magmatism of the Ikh-Mongol Arc system exemplified by the Khantaishir magmatic complex (Lake Zone, south-central Mongolia). *Gondwana Research*, *54*, 122–149. https://doi.org/10.1016/j.gr.2017.10.003

Jia Erken·Tu, E. (2016). *Intrusive magmatic of sequence establishes and tectonic significance of Chonghuer in western part of Aertay Mountain, Xinjiang, (master's thesis)*. Xinjiang University.

Jiang, Y. D., Schulmann, K., Kröner, A., Sun, M., Lexa, O., Janoušek, V., et al. (2017). Neoproterozoic-early Paleozoic Peri-Pacific accretionary evolution of the Mongolian collage system: Insights from geochemical and U-Pb zircon data from the Ordovician sedimentary wedge in the Mongolian Altai. *Tectonics*, *36*(11), 2305–2331. https://doi.org/10.1002/2017tc004533

Jiang, Y. D., Schulmann, K., Sun, M., Štípská, P., Guy, A., Janoušek, V., et al. (2016). Anatexis of accretionary wedge, Pacific-type magmatism, and formation of vertically stratified continental crust in the Altai Orogenic Belt. *Tectonics*, *35*(12), 3095–3118. https://doi.org/10.1002/2016tc004271

Jiang, Y. D., Schulmann, K., Sun, M., Weinberg, R. F., Štípská, P., Li, P. F., et al. (2019). Structural and geochronological constraints on Devonian suprasubduction tectonic switching and Permian collisional dynamics in the Chinese Altai, Central Asia. *Tectonics*, *38*(1), 253–280. https://doi.org/10.1029/2018tc005231

Jiang, Y. D., Štípská, P., Schulmann, K., Aguilar, C., Wang, S., Anczkiewicz, R., et al. (2022). Barrovian and Buchan metamorphic series in the Chinese Altai: P-T-t-D evolution and tectonic implications. *Journal of Metamorphic Geology*, *40*(4), 823–857. https://doi.org/10.1111/jmg.12647

Jiang, Y. D., Štípská, P., Sun, M., Schulmann, K., Zhang, J., Wu, Q. H., et al. (2015). Juxtaposition of Barrovian and migmatite domains in the Chinese Altai: A result of crustal thickening followed by doming of partially molten lower crust. *Journal of Metamorphic Geology*, *33*(1), 45–70. https://doi.org/10.1111/jmg.12110

Jiang, Y. D., Sun, M., Kröner, A., Tumurkhuu, D., Long, X. P., Zhao, G. C., et al. (2012). The high-grade Tseel terrane in SW Mongolia: An early Paleozoic arc system or a Precambrian sliver? *Lithos*, *142*, 95–115. https://doi.org/10.1016/j.lithos.2012.02.016

Jiang, Y. D., Sun, M., Zhao, G. C., Yuan, C., Xiao, W. J., Xia, X. P., et al. (2011a). Precambrian detrital zircons in the Early Paleozoic Chinese Altai: Their provenance and implications for the crustal growth of central Asia. *Precambrian Research*, *189*(1–2), 140–154. https://doi.org/10.1016/j.precamres.2011.05.008

Jiang, Y. D., Sun, M., Zhao, G. C., Yuan, C., Xiao, W. J., Xia, X. P., et al. (2011b). The ~390 Ma high-T metamorphic event in the Chinese Altai: A consequence of ridge-subduction? *American Journal of Science*, *310*(10), 1421–1452. https://doi.org/10.2475/10.2010.08

Jolivet, L., Faccenna, C., Goffé, B., Mattei, M., Rossetti, F., Brunet, C., et al. (1998). Midcrustal shear zones in postorogenic extension: Example from the northern Tyrrhenian Sea. *Journal of Geophysical Research: Solid Earth*, *103*(B6), 12123–12160. https://doi.org/10.1029/97jb03616

Jolivet, L., Sautter, V., Moretti, I., Vettor, T., Papadopoulou, Z., Augier, R., et al. (2021). Anatomy and evolution of a migmatite-cored extensional metamorphic dome and interaction with syn-kinematic intrusions, the Mykonos-Delos-Rheneia MCC. *Journal of Geodynamics*, *144*, 101824. https://doi.org/10.1016/j.jog.2021.101824

Kemp, A. I. S., Hawkesworth, C. J., Collins, W. J., Gray, C. M., Blevin, P. L., & Eimf (2009). Isotopic evidence for rapid continental growth in an extensional accretionary orogen: The Tasmanides, eastern Australia. *Earth and Planetary Science Letters*, *284*(3–4), 455–466. https://doi.org/10.1016/j.epsl.2009.05.011

Kröner, A., Lehmann, J., Schulmann, K., Demoux, A., Lexa, O., Tomurhuu, D., et al. (2010). Lithostratigraphic and geochronological constraints on the evolution of the central Asian orogenic belt in SW Mongolia: Early Paleozoic rifting followed by late Paleozoic accretion. *American Journal of Science*, *310*(7), 523–574. https://doi.org/10.2475/07.2010.01

Laurent-Charvet, S., Charvet, J., Monie, P., & Shu, L. S. (2003). Late Paleozoic strike-slip shear zones in eastern central Asia (NW China): New structural and geochronological data. *Tectonics*, *22*(2), 1009. https://doi.org/10.1029/2001tc901047

Lehmann, J., Schulmann, K., Lexa, O., Corsini, M., Kröner, A., Štípská, P., et al. (2010). Structural constraints on the evolution of the central Asian orogenic belt in SW Mongolia. *American Journal of Science*, *310*(7), 575–628. https://doi.org/10.2475/07.2010.02

Lehmann, J., Schulmann, K., Lexa, O., Závada, P., Štípská, P., Hasalová, P., et al. (2017). Detachment folding of partially molten crust in accretionary orogens: A new magma-enhanced vertical mass and heat transfer mechanism. *Lithosphere*, *9*(6), 889–909. https://doi.org/10.1130/L670.1

Li, D., He, D., Sun, M., & Zhang, L. (2020). The role of arc-arc collision in accretionary orogenesis: Insights from ~320 Ma tectono-sedimentary transition in the Karamaili area, NW China. *Tectonics*, *39*(1), e2019TC005623. https://doi.org/10.1029/2019tc005623

Li, P. F., Sun, M., Rosenbaum, G., Jiang, Y. D., & Cai, K. D. (2016). Structural evolution of zonal metamorphic sequences in the southern Chinese Altai and relationships to Permian transpressional tectonics in the Central Asian Orogenic Belt. *Tectonophysics*, *693*, 277–289. https://doi.org/10.1016/j.tecto.2015.11.035

Li, P. F., Sun, M., Rosenbaum, G., Jourdan, F., Li, S. Z., & Cai, K. D. (2017). Late Paleozoic closure of the Ob-Zaisan ocean along the Irtysh shear zone (NW China): Implications for arc amalgamation and oroclinal bending in the Central Asian Orogenic Belt. *The Geological Society of America Bulletin*, *129*(5–6), 547–569. https://doi.org/10.1130/B31541.1

Li, P. F., Sun, M., Shu, C. T., Yuan, C., Jiang, Y. D., Zhang, L., & Cai, K. D. (2019). Evolution of the central Asian orogenic belt along the Siberian margin from Neoproterozoic-early Paleozoic accretion to Devonian trench retreat and a comparison with Phanerozoic eastern Australia. *Earth-Science Reviews*, *198*, 102951. https://doi.org/10.1016/j.earscirev.2019.102951

Lister, G. S., & Baldwin, S. L. (1993). Plutonism and the origin of metamorphic core complexes. *Geology*, *21*(7), 607–610. https://doi.org/10.1130/0091-7613(1993)021<0607:Patoom>2.3.Co;2

Lister, G. S., & Forster, M. (2009). Tectonic mode switches and the nature of orogenesis. *Lithos*, *113*(1–2), 274–291. https://doi.org/10.1016/j.lithos.2008.10.024

19449194, 2022, 9, Downloaded from https://agupubs.onlinelibrary.wiley.com/doi/10.1029/2021TC007195 by Portail BibCNRS INSU, Wiley Online Library on [06/12/2023]. See the Terms and Conditions (https://onlinelibrary.wiley.com/terms-and-conditions) on Wiley Online Library for rules of use; OA articles are governed by the applicable Creative Commons License

Liu, Y., Hu, Z., Gao, S., Guenther, D., Xu, J., Gao, C., & Chen, H. (2008). In situ analysis of major and trace elements of anhydrous minerals by LA-ICP-MS without applying an internal standard. *Chemical Geology*, *257*(1–2), 34–43. https://doi.org/10.1016/j.chemgeo.2008.08.004

Long, X. P., Sun, M., Yuan, C., Xiao, W. J., & Cai, K. (2008). Early Paleozoic sedimentary record of the Chinese Altai: Implications for its tectonic evolution. *Sedimentary Geology*, *208*(3–4), 88–100. https://doi.org/10.1016/j.sedgeo.2008.05.002

Long, X. P., Sun, M., Yuan, C., Xiao, W. J., Lin, S., Wu, F. Y., et al. (2007). Detrital zircon age and Hf isotopic studies for metasedimentary rocks from the Chinese Altai: Implications for the Early Paleozoic tectonic evolution of the Central Asian Orogenic Belt. *Tectonics*, *26*(5), TC5015. https://doi.org/10.1029/2007TC002128

Long, X. P., Yuan, C., Sun, M., Safonova, I., Xiao, W. J., & Wang, Y. J. (2012). Geochemistry and U-Pb detrital zircon dating of Paleozoic graywackes in East Junggar, NW China: Insights into subduction-accretion processes in the southern central Asian Orogenic Belt. *Gondwana Research*, *21*(2–3), 637–653. https://doi.org/10.1016/j.gr.2011.05.015

Ludwig, K. (2003). *ISOPLOT 3.00: A geochronology toolkit for Microsoft Excel* (p. 70). Berkeley Geochronological Center Special Publication.

Maierová, P., Schulmann, K., Lexa, O., Guillot, S., Štípská, P., Janoušek, V., & Čadek, O. (2016). European Variscan orogenic evolution as an analogue of Tibetan-Himalayan orogen: Insights from petrology and numerical modeling. *Tectonics*, *35*(7), 1760–1780. https://doi.org/10.1002/2015tc004098

Markova, N. G. (1975). *Stratigraphy of the lower and middle paleozoic of western Mongolia, Moscow*. Nauka Press. Transactions of Joint Soviet-Mongolian Scientific Research Geological Expedition.

Morrissey, L. J., Hand, M., Raimondo, T., & Kelsey, D. E. (2014). Long-lived high-T, low-P granulite facies metamorphism in the Arunta Region, central Australia. *Journal of Metamorphic Geology*, *32*(1), 25–47. https://doi.org/10.1111/jmg.12056

Nguyen, H., Hanžl, P., Janoušek, V., Schulmann, K., Ulrich, M., Jiang, Y. D., et al. (2018). Geochemistry and geochronology of Mississippian volcanic rocks from SW Mongolia: Implications for terrane subdivision and magmatic arc activity in the Trans-Altai Zone. *Journal of Asian Earth Sciences*, *164*, 322–343. https://doi.org/10.1016/j.jseaes.2018.06.029

Niu, H. C., Sato, H., Zhang, H. X., Ito, J., Yu, X. Y., Nagao, T., et al. (2006). Juxtaposition of adakite, boninite, high-TiO_2 and low-TiO_2 basalts in the Devonian southern Altay, Xinjiang, NW China. *Journal of Asian Earth Sciences*, *28*(4–6), 439–456. https://doi.org/10.1016/j.jseaes.2005.11.010

Qu, G., & Zhang, J. (1994). Oblique thrust systems in the Altay orogen, China. *Journal of Southeast Asian Earth Sciences*, *9*(3), 277–287. https://doi.org/10.1016/0743-9547(94)90035-3

Schellart, W. P., Lister, G. S., & Jessell, M. W. (2002). Analogue modeling of arc and backarc deformation in the New Hebrides arc and North Fiji Basin. *Geology*, *30*(4), 311–314. https://doi.org/10.1130/0091-7613(2002)030<0311:Amoaab>2.0.Co;2

Sengör, A. M. C., & Natal'in, B. A. (1996). Turkic-type orogeny and its role in the making of the continental crust. *Annual Review of Earth and Planetary Sciences*, *24*(1), 263–337. https://doi.org/10.1146/annurev.earth.24.1.263

Şengör, A. M. C., Natal'in, B. A., & Burtman, V. S. (1993). Evolution of the Altaid tectonic collage and Palaeozoic crustal growth in Eurasia. *Nature*, *364*(6435), 299–307. https://doi.org/10.1038/364299a0

Shaanan, U., Rosenbaum, G., Li, P. F., & Vasconcelos, P. (2014). Structural evolution of the early Permian Nambucca Block (New England Orogen, eastern Australia) and implications for oroclinal bending. *Tectonics*, *33*(7), 1425–1443. https://doi.org/10.1002/2013tc003426

Shan, Q., Niu, H., Yu, X., & Zhang, H. (2005). Geochemistry and zircon U-Pb age of volcanic rocks from the Hanasi basin in the northern Xinjiang and their tectonic significance. *Geochimica*, *34*(4), 315–327. (in Chinese with English abstract).

Shu, T., Jiang, Y., Schulmann, K., Yu, Y., Yuan, C., Wang, S., et al. (2022). Structure, geochronology, and petrogenesis of Permian peraluminous granite dykes in the southern Chinese Altai as indicators of Altai–East Junggar convergence. *GSA Bulletin*, *134*. https://doi.org/10.1130/B36408.1

Soejono, I., Buriánek, D., Janoušek, V., Svojtka, M., Čáp, P., Erban, V., & Ganpurev, N. (2017). A reworked Lake Zone margin: Chronological and geochemical constraints from the Ordovician arc-related basement of the Hovd Zone (Western Mongolia). *Lithos*, *294*, 112–132. https://doi.org/10.1016/j.lithos.2017.08.014

Soejono, I., Burianek, D., Svojtka, M., Zacek, V., Cap, P., & Janousek, V. (2016). Mid-Ordovician and late Devonian magmatism in the Togtokhinshil complex: New insight into the formation and accretionary evolution of the Lake zone (Western Mongolia). *Journal of Geosciences*, *61*(1), 5–23. https://doi.org/10.3190/jgeosci.208

Soejono, I., Čáp, P., Míková, J., Janoušek, V., Buriánek, D., & Schulmann, K. (2018). Early Palaeozoic sedimentary record and provenance of flysch sequences in the Hovd Zone (Western Mongolia): Implications for the geodynamic evolution of the Altai accretionary wedge system. *Gondwana Research*, *64*, 163–183. https://doi.org/10.1016/j.gr.2018.07.005

Soejono, I., Peřestý, V., Schulmann, K., Čopjaková, R., Svojtka, M., Štípská, P., et al. (2021). Structural, metamorphic and geochronological constraints on Palaeozoic multi-stage geodynamic evolution of the Altai accretionary wedge system (Hovd Zone, Western Mongolia). *Lithos*, *396*, 106204. https://doi.org/10.1016/j.lithos.2021.106204

Soldner, J., Štípská, P., Schulmann, K., Yuan, C., Anczkiewicz, R., Sala, D., et al. (2020). Coupling of P–T–t–D histories of eclogite and metagreywacke—Insights to late Ordovician–Silurian crustal folding events recorded in the Beishan Orogen (NW China). *Journal of Metamorphic Geology*, *38*(6), 555–591. https://doi.org/10.1111/jmg.12531

Štípská, P., Chopin, F., Skrzypek, E., Schulmann, K., Pitra, P., Lexa, O., et al. (2012). The juxtaposition of eclogite and mid-crustal rocks in the Orlica-Śnieżnik Dome, Bohemian Massif. *Journal of Metamorphic Geology*, *30*(2), 213–234. https://doi.org/10.1111/j.1525-1314.2011.00964.x

Sun, M., Long, X. P., Cai, K. D., Jiang, Y. D., Wang, B. Y., Yuan, C., et al. (2009). Early Paleozoic ridge subduction in the Chinese Altai: Insight from the abrupt change in zircon Hf isotopic compositions. *Science in China—Series D: Earth Sciences*, *52*(9), 1345–1358. https://doi.org/10.1007/s11430-009-0110-3

Sun, M., Yuan, C., Xiao, W. J., Long, X. P., Xia, X. P., Zhao, G. C., et al. (2008). Zircon U-Pb and Hf isotopic study of gneissic rocks from the Chinese Altai: Progressive accretionary history in the early to middle Palaeozoic. *Chemical Geology*, *247*(3–4), 352–383. https://doi.org/10.1016/j.chemgeo.2007.10.026

Tirel, C., Brun, J.-P., & Burov, E. (2008). Dynamics and structural development of metamorphic core complexes. *Journal of Geophysical Research: Solid Earth*, *113*(B4), B04403. https://doi.org/10.1029/2005jb003694

Tomascak, P. B., Krogstad, E. J., & Walker, R. J. (1996). U-Pb monazite geochronology of granitic rocks from Maine: Implications for Late Paleozoic tectonics in the northern Appalachians. *The Journal of Geology*, *104*(2), 185–195. https://doi.org/10.1086/629813

Tong, Y., Wang, T., Hong, D., Liu, X., & Han, B. (2005). Zircon U–Pb age of syn-orogenic Tielieke pluton in the Western part of Altay orogenic belt and its structural implications. *Acta Geoscientica Sinica*, *26*(z1), 74–77. (in Chinese with English abstract).

Tong, Y., Wang, T., Kovach, V. P., Hong, D. W., & Han, B. F. (2006). Age and origin of the Takeshiken postorogenic alkali-rich intrusive rocks in southern Altai, near the Mongolian border in China and its implications for continental growth. *Acta Petrologica Sinica*, *22*(5), 1267–1278. (in Chinese with English abstract).

19449194, 2022, 9, Downloaded from https://agupubs.onlinelibrary.wiley.com/doi/10.1029/2021TC007195 by Portail BibCNRS INSU, Wiley Online Library on [06/12/2023]. See the Terms and Conditions (https://onlinelibrary.wiley.com/terms-and-conditions) on Wiley Online Library for rules of use; OA articles are governed by the applicable Creative Commons License

Wan, B., Xiao, W. J., Zhang, L. C., Windley, B. F., Han, C. M., & Quinn, C. D. (2011). Contrasting styles of mineralization in the Chinese Altai and East Junggar, NW China: Implications for the accretionary history of the southern Altaids. *Journal of the Geological Society*, *168*(6), 1311–1321. https://doi.org/10.1144/0016-76492011-021

Wan, B., Zhang, L. C., & Xiang, P. (2010). The Ashele VMS-type Cu-Zn deposit in Xinjiang, NW China formed in a rifted arc setting. *Resource Geology*, *60*(2), 150–164. https://doi.org/10.1111/j.1751-3928.2010.00122.x

Wang, S., Jiang, Y., Weinberg, R., Schulmann, K., Zhang, J., Li, P., et al. (2021). Flow of Devonian anatectic crust in the accretionary Altai Orogenic Belt, central Asia: Insights into horizontal and vertical magma transfer. *The Geological Society of America Bulletin*, *133*(11–12), 2501–2523. https://doi.org/10.1130/B35645.1

Wang, S., Xu, K., Huang, Y., Kong, L., Qi, Y., Song, S., et al. (2018). Permian deformational history of Western Chinese Altai Orogenic Belt: Insights from structural and monazite U-Pb data. *Geotectonica et Metallogenia*, *42*(5), 798–811. (in Chinese with English abstract). https://doi.org/10.16539/j.ddgzyckx.2018.04.013

Wang, T., Hong, D. W., Jahn, B. M., Tong, Y., Wang, Y. B., Han, B. F., & Wang, X. X. (2006). Timing, petrogenesis, and setting of Paleozoic synorogenic intrusions from the Altai Mountains, northwest China: Implications for the tectonic evolution of an accretionary orogen. *The Journal of Geology*, *114*(6), 735–751. https://doi.org/10.1086/507617

Wang, Y. J., Yuan, C., Long, X. P., Sun, M., Xiao, W. J., Zhao, G. C., et al. (2011). Geochemistry, zircon U-Pb ages and Hf isotopes of the Paleozoic volcanic rocks in the northwestern Chinese Altai: Petrogenesis and tectonic implications. *Journal of Asian Earth Sciences*, *42*(5), 969–985. https://doi.org/10.1016/j.jseaes.2010.11.005

Wei, C. J., Clarke, G., Tian, W., & Qiu, L. (2007). Transition of metamorphic series from the Kyanite-to andalusite-types in the Altai orogen, Xinjiang, China: Evidence from petrography and calculated KMnFMASH and KFMASH phase relations. *Lithos*, *96*(3–4), 353–374. https://doi.org/10.1016/j.lithos.2006.11.004

White, A. J. R., & Chappell, B. W. (1988). Some supracrustal (S-type) granites of the Lachlan Fold Belt. *Transactions of the Royal Society of Edinburgh Earth Sciences*, *79*(2–3), 169–181. https://doi.org/10.1017/S026359330001419X

Wickham, S. M., & Oxburgh, E. R. (1986). A rifted tectonic setting for Hercynian high-thermal gradient metamorphism in the Pyrenees. *Tectonophysics*, *129*(1–4), 53–69. https://doi.org/10.1016/0040-1951(86)90245-3

Wiedenbeck, M., Allé, P., Corfu, F., Griffin, W. L., Meier, M., Oberli, F., et al. (1995). Three natural zircon standards for U-Th-Pb, Lu-Hf, trace element and REE analyses. *Geostandards and Geoanalytical Research*, *19*(1), 1–23. https://doi.org/10.1111/j.1751-908X.1995.tb00147.x

Windley, B. F., Alexeiev, D., Xiao, W. J., Kröner, A., & Badarch, G. (2007). Tectonic models for accretion of the central Asian Orogenic Belt. *Journal of the Geological Society*, *164*(1), 31–47. https://doi.org/10.1144/0016-76492006-022

Windley, B. F., Kröner, A., Guo, J. H., Qu, G. S., Li, Y. Y., & Zhang, C. (2002). Neoproterozoic to Paleozoic geology of the Altai orogen, NW China: New zircon age data and tectonic evolution. *The Journal of Geology*, *110*(6), 719–737. https://doi.org/10.1086/342866

Windley, B. F., & Xiao, W. J. (2018). Ridge subduction and slab windows in the Central Asian Orogenic Belt: Tectonic implications for the evolution of an accretionary orogen. *Gondwana Research*, *61*, 73–87. https://doi.org/10.1016/j.gr.2018.05.003

Wolfram, L. C., Weinberg, R. F., Nebel, O., Hamza, K., Hasalova, P., Mikova, J., & Becchio, R. (2019). A 60-Myr record of continental back-arc differentiation through cyclic melting. *Nature Geoscience*, *12*(3), 215–219. https://doi.org/10.1038/s41561-019-0298-6

Wong, K., Sun, M., Zhao, G. C., Yuan, C., & Xiao, W. J. (2010). Geochemical and geochronological studies of the Alegedayi Ophiolitic complex and its implication for the evolution of the Chinese Altai. *Gondwana Research*, *18*(2–3), 438–454. https://doi.org/10.1016/j.gr.2010.01.010

Wu, L. (2018). *Study and comparison of the typical stratigraphical sections of the Devonian-Carboniferous in Eastern Junggar, (Master's thesis). Xi'an*. Chang'an University.

Xiao, W. J., Windley, B. F., Han, C. M., Liu, W., Wan, B., Zhang, J., et al. (2018). Late Paleozoic to early Triassic multiple roll-back and oroclinal bending of the Mongolia collage in Central Asia. *Earth-Science Reviews*, *186*, 94–128. https://doi.org/10.1016/j.earscirev.2017.09.020

Xiao, W. J., Windley, B. F., Hao, J., & Zhai, M. G. (2003). Accretion leading to collision and the Permian Solonker suture, Inner Mongolia, China: Termination of the Central Asian Orogenic Belt. *Tectonics*, *22*(6), 1069. https://doi.org/10.1029/2002TC001484

Xiao, W. J., Windley, B. F., Sun, S., Li, J. L., Huang, B. C., Han, C. M., et al. (2015). A tale of amalgamation of three Permo-Triassic collage systems in Central Asia: Oroclines, sutures, and terminal accretion. *Annual Review of Earth and Planetary Sciences*, *43*(1), 477–507. https://doi.org/10.1146/annurev-earth-060614-105254

Xiao, W. J., Windley, B. F., Yuan, C., Sun, M., Han, C. M., Lin, S. F., et al. (2009). Paleozoic multiple subduction-accretion processes of the Southern Altaids. *American Journal of Science*, *309*(3), 221–270. https://doi.org/10.2475/03.2009.02

Xu, J. F., Castillo, P. R., Chen, F. R., Niu, H. C., Yu, X. Y., & Zhen, Z. P. (2003). Geochemistry of Late Paleozoic mafic igneous rocks from the Kuerti area, Xinjiang, northwest China: Implications for backarc mantle evolution. *Chemical Geology*, *193*(1–2), 137–154. https://doi.org/10.1016/S0009-2541(02)00265-6

Xu, K., Jiang, Y., Wang, S., Shu, T., Li, Z., Collett, S., et al. (2021). Multi-phase tectonothermal evolution in the SE Chinese Altai, central Asia: Structures, U-Pb monazite ages and tectonic implications. *Lithos*, *392*, 106148. https://doi.org/10.1016/j.lithos.2021.106148

Yu, Y., Sun, M., Long, X. P., Li, P. F., Zhao, G. C., Kröner, A., et al. (2017). Whole-rock Nd-Hf isotopic study of I-type and peraluminous granitic rocks from the Chinese Altai: Constraints on the nature of the lower crust and tectonic setting. *Gondwana Research*, *47*, 131–141. https://doi.org/10.1016/j.gr.2016.07.003

Yuan, C., Sun, M., Xiao, W., Li, X., Chen, H., Lin, S., et al. (2007). Accretionary orogenesis of the Chinese Altai: Insights from Paleozoic granitoids. *Chemical Geology*, *242*(1–2), 22–39. https://doi.org/10.1016/j.chemgeo.2007.02.013

Zeng, Q., Chen, G., Wang, H., & Shan, Q. (2007). Geochemical characteristic, SHRIMP zircon U-Pb dating and tectonic implication for granitoids in Chonghuer basin, Altai, Xinjiang. *Acta Petrologica Sinica*, *23*(8), 1921–1932. (in Chinese with English abstract).

Zhang, C., Zhang, X., Santosh, M., Liu, D. D., Ma, C., Zeng, J. H., et al. (2020). Zircon Hf-O-Li isotopes of granitoids from the central Asian Orogenic Belt: Implications for supercontinent evolution. *Gondwana Research*, *83*, 132–140. https://doi.org/10.1016/j.gr.2020.02.003

Zhang, J., Sun, M., Schulmann, K., Zhao, G. C., Wu, Q. H., Jiang, Y. D., et al. (2015). Distinct deformational history of two contrasting tectonic domains in the Chinese Altai: Their significance in understanding accretionary orogenic process. *Journal of Structural Geology*, *73*, 64–82. https://doi.org/10.1016/j.jsg.2015.02.007

Zhang, Z., Mao, J., Cai, J., Kusky, T. M., Zhou, G., Yan, S., & Zhao, L. (2008). Geochemistry of picrites and associated lavas of a Devonian island arc in the northern Junggar terrane, Xinjiang (NW China): Implications for petrogenesis, arc mantle sources and tectonic setting. *Lithos*, *105*(3–4), 379–395. https://doi.org/10.1016/j.lithos.2008.05.013

Zhao, T., Zhu, Z., Han, Q., & Zheng, J. (2018). Age, petrogenesis and geological significance of the Northern Qibaroi mafic intrusion in Altay, China. *Geological Review*, *64*(1), 247–260. (in Chinese with English abstract). https://doi.org/10.16509/j.georeview.2018.01.019

19449194, 2022, 9, Downloaded from https://agupubs.onlinelibrary.wiley.com/doi/10.1029/2021TC007195 by Portail BibCNRS INSU, Wiley Online Library on [06/12/2023]. See the Terms and Conditions (https://onlinelibrary.wiley.com/terms-and-conditions) on Wiley Online Library for rules of use; OA articles are governed by the applicable Creative Commons License

Zheng, J., Zhao, T., Tang, Z., Han, Q., Wang, T., Li, C., et al. (2016). Geochemical characters, LA-ICP-MS zircon U-Pb dating of Tielielike rock in Western Altay mountains of Xinjiang and its geological significance. *Xinjiang Geology*, *34*(01), 54–61. (in Chinese with English abstract).

Zong, K. Q., Klemd, R., Yuan, Y., He, Z. Y., Guo, J. L., Shi, X. L., et al. (2017). The assembly of Rodinia: The correlation of early Neoproterozoic (ca. 900 Ma) high-grade metamorphism and continental arc formation in the southern Beishan Orogen, southern Central Asian Orogenic Belt (CAOB). *Precambrian Research*, *290*, 32–48. https://doi.org/10.1016/j.precamres.2016.12.010

19449194, 2022, 9, Downloaded from https://agupubs.onlinelibrary.wiley.com/doi/10.1029/2021TC007195 by Portail BibCNRS INSU, Wiley Online Library on [06/12/2023]. See the Terms and Conditions (https://onlinelibrary.wiley.com/terms-and-conditions) on Wiley Online Library for rules of use; OA articles are governed by the applicable Creative Commons License